ANNUAL REVIEWS

Annual Review of Chemical and Biomolecular Engineering

Wearable and Implantable Soft Bioelectronics: Device Designs and Material Strategies

Sung-Hyuk Sunwoo,[1,2,*] Kyoung-Ho Ha,[3,*] Sangkyu Lee,[1,*] Nanshu Lu,[3,4] and Dae-Hyeong Kim[1,2,5]

[1]Center for Nanoparticle Research, Institute for Basic Science (IBS), Seoul 08826, Republic of Korea; email: dkim98@snu.ac.kr

[2]School of Chemical and Biological Engineering, Institute of Chemical Processes, Seoul National University, Seoul 08826, Republic of Korea

[3]Department of Mechanical Engineering, The University of Texas at Austin, Texas 78712, USA; email: nanshulu@utexas.edu

[4]Center for Mechanics of Solids, Structures and Materials, Department of Aerospace Engineering and Engineering Mechanics, Department of Biomedical Engineering, and Texas Material Institute, The University of Texas at Austin, Texas 78712, USA

[5]Department of Materials Science and Engineering, Seoul National University, Seoul 08826, Republic of Korea

Annu. Rev. Chem. Biomol. Eng. 2021. 12:359–91

The *Annual Review of Chemical and Biomolecular Engineering* is online at chembioeng.annualreviews.org

https://doi.org/10.1146/annurev-chembioeng-101420-024336

*These authors contributed equally to this article

Keywords

flexible electronics, stretchable electronics, soft materials, wearable devices, implantable devices, health monitoring, point-of-care therapy

Abstract

High-performance wearable and implantable devices capable of recording physiological signals and delivering appropriate therapeutics in real time are playing a pivotal role in revolutionizing personalized healthcare. However, the mechanical and biochemical mismatches between rigid, inorganic devices and soft, organic human tissues cause significant trouble, including skin irritation, tissue damage, compromised signal-to-noise ratios, and limited service time. As a result, profuse research efforts have been devoted to overcoming these issues by using flexible and stretchable device designs and soft materials. Here, we summarize recent representative research and technological advances for soft bioelectronics, including conformable and stretchable device designs, various types of soft electronic materials, and surface coating and treatment methods. We also highlight applications of these strategies to emerging soft wearable and implantable devices. We conclude with some current limitations and offer future prospects of this booming field.

1. INTRODUCTION

Unlike conventional machines, such as cars or robots, that are continuously monitored by thousands of sensors, the human body as a soft machine is rarely monitored at present, except for special cases in patients, disabled persons (1), or military personnel (2). In fact, our body is constantly radiating highly personalized electrical, mechanical, thermal, and biochemical signals indicating our health, emotions, and actions (3). These signals are imperative for an objective evaluation of current body status, an accurate prediction of its future, and the safe merging and/or collaboration between living and nonliving machines. As a result, digitizing our body is as important as keeping a car or a robot monitored and connected, with privacy preserved, of course. This rationale has sparked the recent surge in wearables and implantables, the forefront of the Internet of things in, e.g., healthcare (4, 5), sports (6), and human–machine interaction (7) (**Figure 1*a***).

Possible applications of wearables include medical and healthcare monitoring and diagnostics (8, 9), transdermal drug delivery (10), fitness monitoring (11), military performance trackers (2, 12) and wearable robots (13, 14), smart apparel and footwear in fashion and sports (15–17), workplace safety and manufacturing (18, 19), and electrical stimulation and thermotherapy (20). In contrast, current implantable devices are used mainly for acute or chronic diseases (21–23), such as pacemakers (24, 25), cardiovascular stents (26, 27), defibrillators (28), neural prosthetics (29–31), intraocular lenses (32, 33), hearing aids (34), drug delivery systems (35), and so on (36).

Because the human body has a soft, curvilinear, and multimodal nature, safe, intimate, and long-term integration of a device with the human body calls for soft, biocompatible, and multifunctional devices. In this manner, the current rigid bioelectronics may induce inflammatory responses (37, 38) and exhibit unstable device functionalities, particularly under long-term integration on the target organ. This is due largely to the mismatches in the mechanical properties (**Figure 1*b***) and chemical compositions between soft biological tissues and conventional rigid electronics. The mechanical mismatch and chemical disparity affect chronic biocompatibility and decrease bioelectronic performance.

The mechanical stiffness of conventional bioelectronics can induce side effects on the soft tissues in contact with them, in both wearable and implantable applications. For example, the rigidity of a wearable device (39) mounted on the skin evokes discomfort and skin irritation (40, 41). Because stiff and flat electronics cannot intimately follow the contour of soft and curvilinear skin, the pressure is concentrated in a localized area, and friction between the device and the skin may result in skin rashes and allergic reactions (**Figure 1*c***, *left*). Moreover, rigid and flat bioelectronics cannot make conformal contact with soft and curvilinear skin, and such incomplete contact lowers bioelectronic performance owing to high impedance and low signal-to-noise ratio (42, 43).

Similar to the case of wearable bioelectronics, the rigidity of implantable bioelectronics can cause inflammatory reactions, particularly in their long-term implantation (44, 45). Natural micromotions of the biological tissue can accumulate stress on the tissue interfacing with rigid devices (46, 47) (**Figure 1*d***). Such stress can lead to inflammatory reactions that replace normal tissues near the device with scar tissue. Accordingly, this thick, fibrous scar tissue lowers the sensing and stimulating performance of the implanted bioelectronics by blocking the flow of electrical signals between the target tissue and the electronics.

In addition, unlike conventional wearable and implantable bioelectronics that consist of metal and/or inorganic materials, biological tissues are hydrophilic, ion rich, and fluidic. This difference in chemical compositions limits the long-term biocompatibility and performance of bioelectronics (48). For example, natural flows of air and moisture to the skin can be blocked by wearable bioelectronics covering the skin. This impermeable condition is favorable to bacterial growth and propagation, which can cause infection and skin irritation. Also, the accumulation of sweat, oil, and

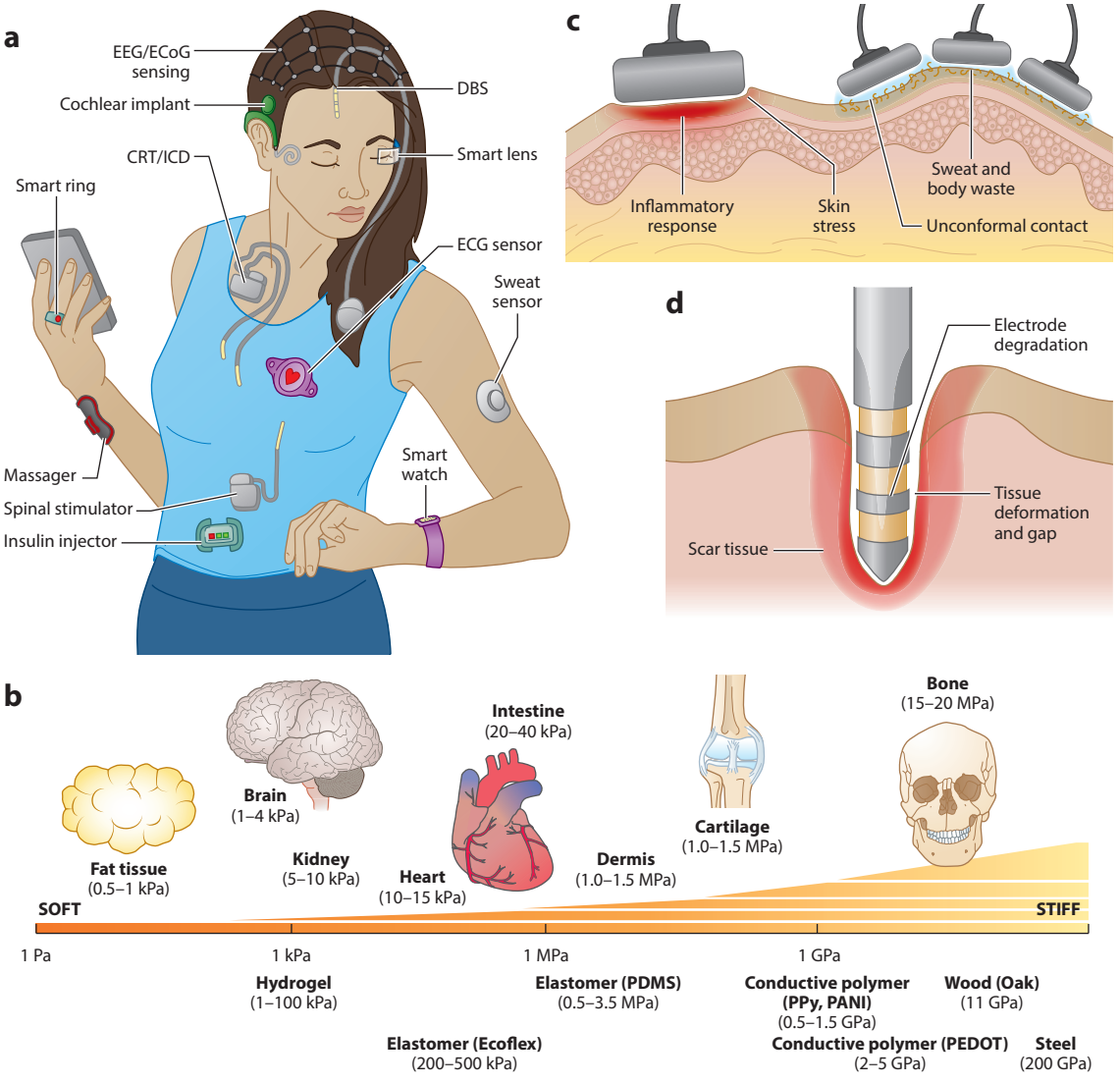

Figure 1

Current wearable/implantable bioelectronics and their limitations. (*a*) Conventional wearable/implantable bioelectronics for healthcare, sports, and human–machine interfaces. (*b*) Mechanical characteristic differences between soft biological tissues and device materials, in terms of Young's modulus. Drawbacks of conventional (*c*) wearable and (*d*) implantable bioelectronics for chronic application. Abbreviations: CRT, cardiac resynchronization treatment; DBS, deep-brain stimulator; ECG, electrocardiogram; ECoG, electrocorticogram; EEG, electroencephalogram; ICD, implantable cardioverter-defibrillator; PANI, polyaniline; PDMS, polydimethylsiloxane; PEDOT, poly(ethylene dioxythiphene); PPy, polypyrrole.

other body wastes between the skin and bioelectronics interferes with sensing and stimulation of the bioelectronics (**Figure 1*c***, *right*).

Meanwhile, the difference in chemical composition between the implantable bioelectronics and target tissue can attenuate the ionic current flow and stimulate inflammatory reactions. Less adhesion of the biological tissue onto the hydrophobic surface of the implantable bioelectronics aggravates such situations. Moreover, the complex reaction of immune cells, enzymes, radicals,

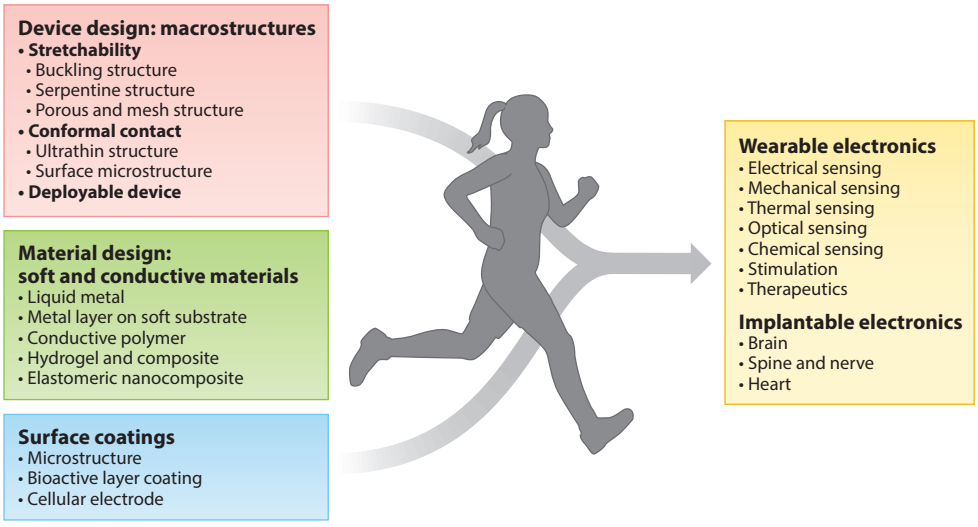

Figure 2

Strategies for long-term wearable and implantable bioelectronics, including device design, material design, and surface coatings.

and reactive oxygen species gradually degrades bioelectronics materials, including the encapsulation layers, eventually leading to device failure (49) (**Figure 1*d***). In addition, increased impedance owing to scar tissue generation and potential leakage of current from the device owing to material degradation can cause undesired biochemical reactions, such as water electrolysis or radical formation (50).

To address these discrepancies between soft biological tissues and conventional rigid bioelectronics, both the scientific community and the industry have turned their attention to soft bioelectronics. The number of publications on soft wearable or implantable electronics on Web of Science has grown exponentially, from 119 in 2000 to 7,493 in 2019. According to IDTechEx, the market size for flexible electronics in healthcare will exceed $8.3 billion by 2030. These expectations and investments have sprung up numerous novel device designs, advanced soft materials, and surface-coating strategies that have been adopted to make breakthroughs in maximizing the long-term reliability and performance of wearable and implantable bioelectronics. Here, we review such strategies to develop soft wearable and implantable bioelectronics (51, 52) (**Figure 2**).

This review is organized as follows (**Figure 2**). First, we introduce novel device design strategies to reduce the mechanical mismatch between bioelectronics and tissue. Then, we discuss soft materials for advanced wearable and implantable bioelectronics, such as liquid metal, nanotubes and nanowires, conductive polymers, conductive hydrogels, and elastomeric nanocomposites. Additionally, we review surface modification strategies that can reduce inflammatory responses for chronic implantation of devices, followed by representative examples of application of these strategies to wearable and implantable bioelectronics. Finally, we discuss unresolved issues for the widespread application of soft wearable and implantable bioelectronics to clinics and healthcare industries.

2. DEVICE DESIGN STRATEGIES

Conventional, intrinsically stiff electronic materials, such as silicon, III-V compound semiconductors, and metals, can be tuned for structural properties suitable for bio-integration through

mechanics-guided geometric and configurational designs. Such properties include bendability, stretchability, conformability to curvilinear tissue surfaces, and 3D deployability to couple with tissues or guide tissue growth (53). Although bendability and stretchability are well covered in previous reviews (54–57), conformability and deployability are not. In this section, we briefly summarize the most recent progress on stretchable designs and then focus on conformable and deployable designs that have been directly employed in bio-integrated devices.

2.1. Designed Stretchability

Stretchability is crucial for bio-integrated electronics for the following two reasons. First, because most microelectronics are fabricated to be planar, stretchability is required to conform a planar device to undevelopable surfaces (i.e., surfaces with nonzero Gaussian curvature) of bio-tissues and organs. Second, because most bio-tissues are soft and stretchable, only stretchable devices that can deform together with the tissues are able to maintain functionality as well as form an intimate and low-stress bioelectronics interface. Therefore, many design strategies have been applied to achieve stretchable bioelectronics using high-modulus materials, including out-of-plane buckling, island-plus-serpentine, or filamentary serpentine designs and fractal-, microcrack-, or kirigami-inspired designs. In the following, we review one example from each category.

A standard method for fabricating out-of-plane buckling structure is to first laminate a stiff thin-film device on a prestretched soft substrate and then release the substrate to recover. It is well-known that nanocrystalline gold thin film is actually very brittle [e.g., ruptures at a tensile strain of 1% (58)]. However, when electrodes of 100-nm-thick gold on 1-μm-thick polyethylene terephthalate were transferred on a 200% prestretched acrylic elastomer and released, the spontaneously formed wrinkled gold electrodes could survive tensile strains of up to 120% (59) (**Figure 3*a***). As a result, the stretchable gold electrode could be successfully applied to a rat's bladder to monitor the voiding function with a volume change from 71% to 100%. **Figure 3*b*** proposes that compared with compression-induced wrinkled (*top*) or buckled (*middle*) ribbons, buckled ribbons formed with guiding tripods (*bottom*) undergo the least strain because of the larger curve radius at the peaks and valleys (60). As a result, a buckled gold electrode with tripods and 50% prestretch could be stretched up to 130% without any notable increase in resistance.

However, out-of-plane buckled ribbons or films yield a rough device surface, which impedes intimate contact between the device and the soft bio-tissue. Therefore, after 2010, in-plane meandering ribbons, called serpentines, became the commonly adopted design for stretchable bioelectronics. Serpentines are essentially 2D springs that elongate through ribbon rotation and twisting, helping to reduce the intrinsic strains in a material (61, 62). Serpentine mechanics has been studied extensively (63–67). There are a few variations of serpentine-enabled stretchable electronics, including the design of island device plus serpentine interconnects (**Figure 3*c***), the filamentary serpentine ribbons (**Figure 3*d***), the fractal serpentine pattern (**Figure 3*e***), and the serpentine network with triangular lattice (**Figure 3*f***). As out-of-plane buckling and twisting upon stretch are very effective in releasing strain in serpentines (65), Xu et al. (68) engineered a dense array of pyramids on the substrate and formed a microfluidic chamber to enable the serpentine interconnects to freely deform in the created 3D space with minimized adhesion or friction (**Figure 3*c***). Based on finite element method simulation, such freestanding serpentines have an elastic stretchability of 167%, compared with only 17% for the fully bonded serpentines. Using such highly stretchable interconnects, this patch could incorporate multiple off-the-shelf integrated circuits (ICs) and hence achieved various functions via a so-called cut-and-paste method (69) (**Figure 3*d***). The one-time stretchability of the e-tattoo was more than 55%, and the cyclability was more than 10,000 times under an applied strain of 20%. A multilayer wireless e-tattoo fabricated via an upgraded cut–solder–paste method could incorporate rigid ICs but stayed stretchable up to 30% (70).

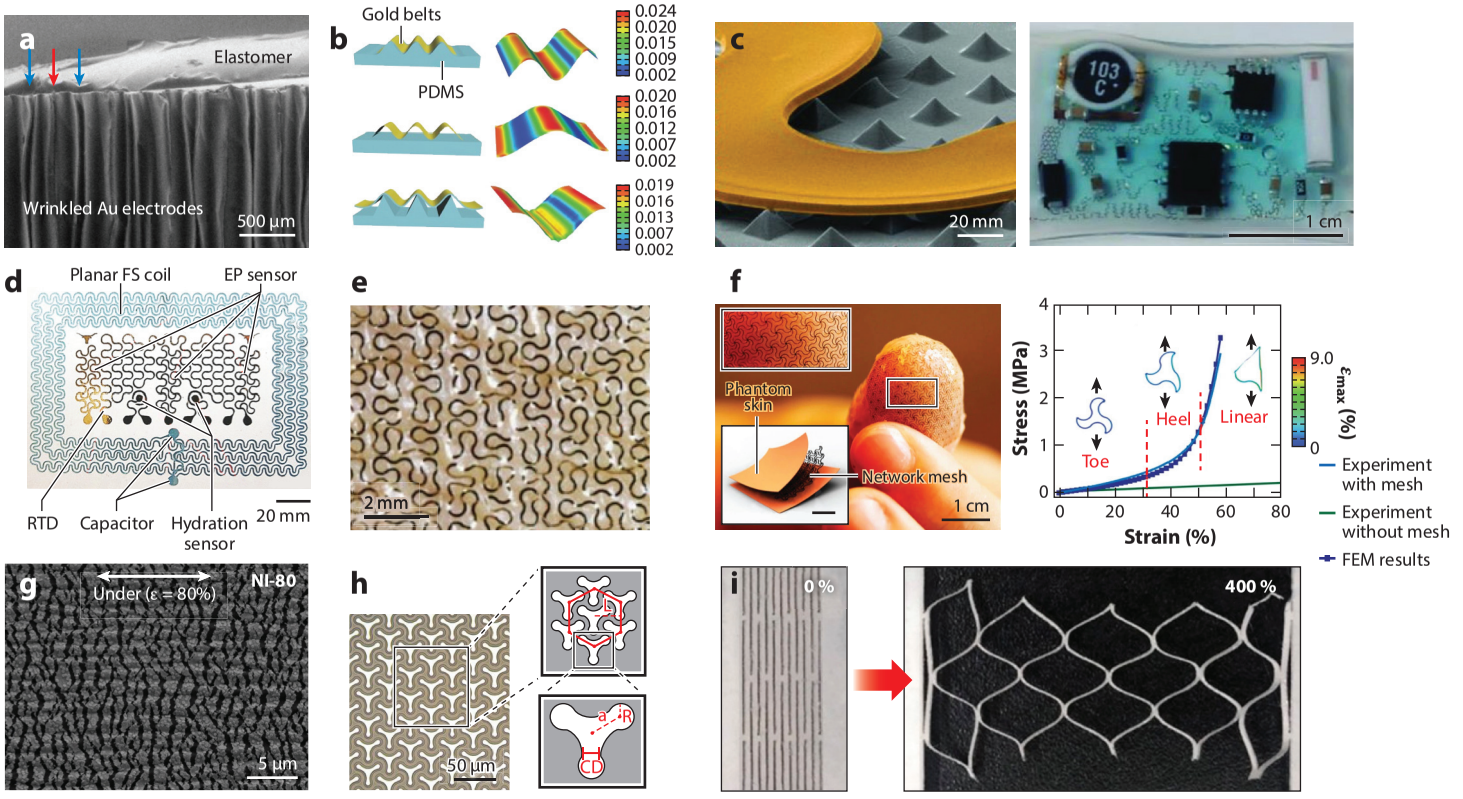

Figure 3

Device design for stretchability. (*a*) SEM image of a wrinkled gold/PET electrode on an acrylic elastomer (adapted with permission from Reference 59; copyright 2020 AAAS). (*b*) Schematics and FEM of wrinkled, buckled, and tripod-guided-buckled gold ribbons as stretchable electrodes (adapted with permission from Reference 60; copyright 2015 Wiley-VCH). (*c*) Colorized SEM image of serpentine interconnects on a pyramid-patterned substrate (*left*). The serpentine interconnect can buckle and twist freely in a thin elastomeric microfluidic enclosure (*right*) (adapted with permission from Reference 68; copyright 2014 AAAS). (*d*) Optical image of a multiparametric all-filamentary-serpentine e-tattoo (adapted with permission from Reference 69; copyright 2015 Wiley-VCH). (*e*) Optical image of a highly stretchable gold electrode on skin (adapted with permission from Reference 71; copyright 2014 Springer Nature). (*f*) Optical image of a skin-like composite with serpentine 2D triangular lattice wrapped onto the tip of a thumb (*left*). Experimental (*line*) and FEM (*line plus square*) results for the stress–strain response (*right*) (adapted with permission from Reference 74; copyright 2015 Springer Nature). (*g*) SEM image of a microcracked gold electrode under a horizontal tensile strain of 60% (adapted with permission from Reference 75; copyright 2014 ACS). (*h*) Micrograph of stretchable electrodes with a Y-shaped motif pattern (adapted with permission from Reference 77; copyright 2019 AAAS). (*i*) Image of a kirigami-patterned aluminum-in-Ecoflex electrode before and after 400% stretching (adapted with permission from Reference 78; copyright 2017 ACS). Abbreviations: CD, critical dimension; EP, electrophysiology; FEM, finite element modeling; FS, filamentary serpentine; PDMS, polydimethylsiloxane; PET, polyethylene terephthalate; RTD, resistance temperature detector; SEM, scanning electron microscopy.

Compared with simple serpentine patterns, fractal serpentine designs gained larger areal filling factors and supported various deformation modes, including biaxial and radial deformation (71) (**Figure 3*e***). Stretchability could be enhanced as the hierarchy of self-similar serpentines increased (72, 73). Fractal-enabled, highly stretchable epidermal electronics have been used for joule heating, temperature sensing, and ECG measurement. Although serpentines provide sufficient stretchability, their mechanical properties do not precisely match the nonlinear behavior of bio-tissues. As a result, a 2D triangular lattice with horseshoe serpentines has been designed, the stress/strain response of which can be tailored to fully overlap with that of human skin (74) (**Figure 3*f***).

To further enhance the areal filling factor, microcrack- and kirigami-based stretchable patterns emerged as new designs to accommodate the applied stretch. Liu et al. (75) fabricated microcracked gold electrodes that could be stretched up to 120% and applied them as soft electroencephalogram (EEG) and electrocorticogram (ECoG) sensors (**Figure 3*g***). However, the microcracked electrodes suffered from large variations of resistance with stretch. Moreover, owing to fatigue, microcracks gradually develop into macrocracks, which fail the device after a limited number of cycles. To overcome these limitations, Vachicouras et al. (76, 77) patterned Y-shaped motifs on films inspired by microcracked gold films (**Figure 3*h***). Notably, the blunt tips of each branch helped suppress crack initiation and hence secured mechanical and electrical stability. This electrode was stretchable up to 60% and remained electrically conductive under 1,000,000 cycles of 10% stretching. When the cracks are long enough and the solid segments are narrow enough, the design can be called kirigami inspired; such designs can enable gigantic stretchability when the cracks (now called slits) open up. Slit number, length, location, and direction can modulate stretchability. For example, Jang et al. (78) made cuts on an elastomer with embedded aluminum foil and achieved a stretchability of 400% and durability of 1,000 cycles at 300% strain (**Figure 3*i***).

2.2. Designed Conformability

Because tissue surfaces are never perfectly flat, conformable contact between bioelectronics and tissue surfaces is crucial for low contact impedance; efficient mass, heat, or light transfer; suppressed relative motion; and hence reduced motion artifacts. Not all stretchable devices can adhere perfectly to curvilinear skin surfaces. Existing mechanics analyses (79–82) have pointed out the following five factors that dictate conformability: tissue surface roughness, tissue modulus, device thickness and stiffness, and device–tissue interface adhesion. Given a target tissue, surface roughness and modulus are predetermined. Hence, it is critical to design thin and soft devices with strong adhesion to achieve ideal conformability (83–85).

Figure 4*a* plots a 2D schematic of the mechanics model of bioelectronics conformability and the corresponding analytical result (80). Nonconformable and fully conformable contacts correspond to a conformability of 0 and 1, respectively. The model took tissue roughness and modulus as inputs and device thickness, stiffness, and adhesion as variables. For a given tissue surface with 250-μm wavelength and 50-μm amplitude, a tissue and device plane strain modulus of 92 kPa, and a given van der Waals interface adhesion of 50 mJ/m^2, the model predicts that only devices thinner than 7.5 μm can achieve full conformability with the tissue. As the device thickness increases, its conformability drops abruptly from 1 to below 0.23 owing to mechanical pull-in instability. Such a prediction is highly consistent with the experimental observation shown in **Figure 4*b***, where Ecoflex layers of various thicknesses (*blue colored*) were placed on a skin replica (86). No conformability could be observed when the Ecoflex was 36 μm thick, while full conformability was achieved at only 5-μm thickness. As the device thickness decreased from 500 μm to 5 μm, the skin–electrode contact impedance also decreased from 91.8 kΩ to 19.6 kΩ, and the background noise dropped from 250 μV_{RMS} to 12 μV_{RMS}.

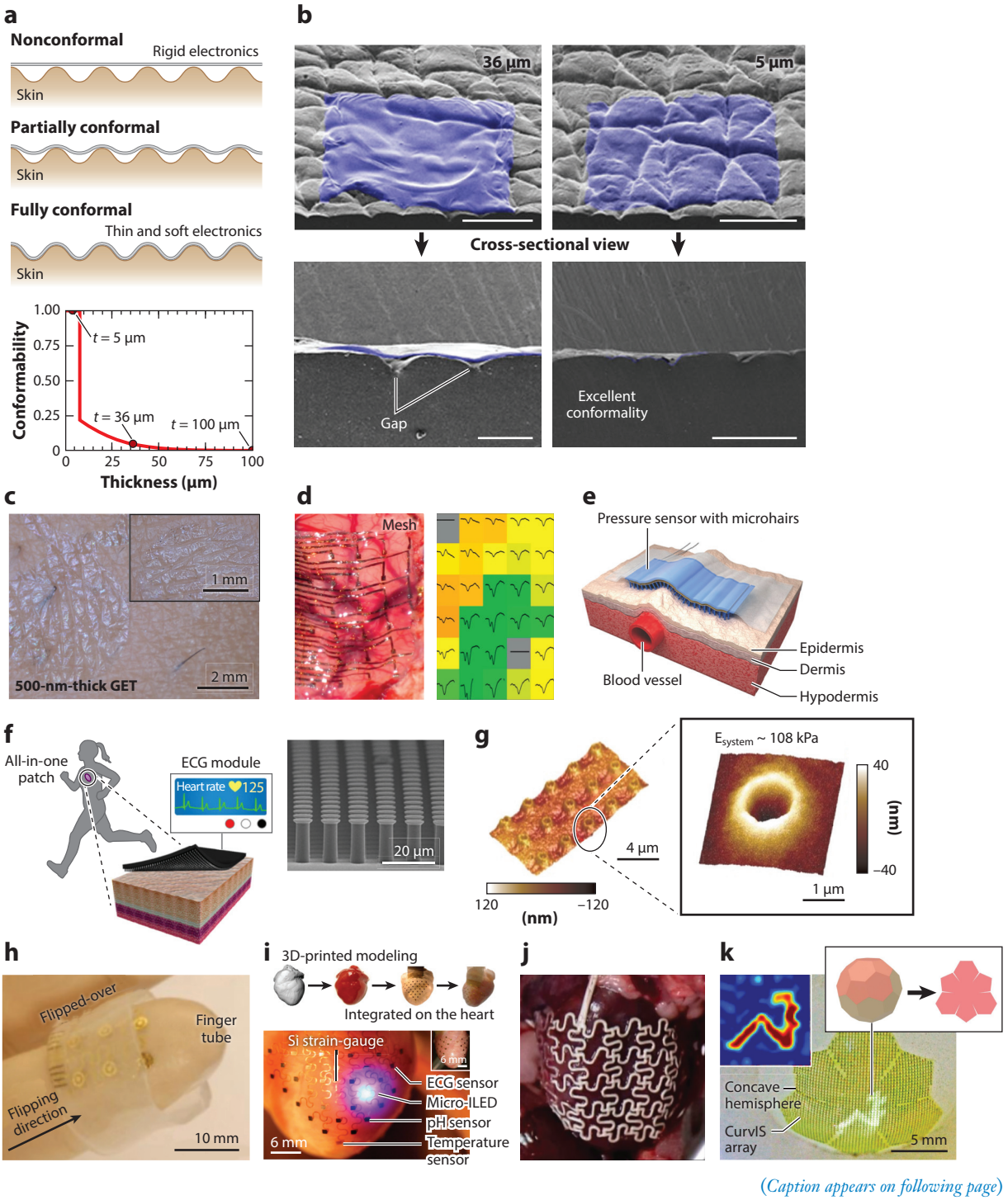

(Caption appears on following page)

Figure 4 (*Figure appears on preceding page*)

Device design for bio-conformability. (*a*) Schematic illustration of the mechanics model of bio-conformability (*top*) and corresponding analytical results (*bottom*) (adapted with permission from Reference 80; copyright 2016 ASME). (*b*) Angled and cross-sectional SEM images showing the contact between a silicone replica of the human skin and different thicknesses of Ecoflex membranes (left: 36 μm, right: 5 μm) (adapted with permission from Reference 86; copyright 2013 Wiley-VCH). (*c*) Optical image of a 500-nm-thick transparent GET sensor fully conformable to the human skin (adapted with permission from Reference 87; copyright 2018 Springer Nature). (*d*) Optical image of a 2.5-μm-thick electrode array conformally contacted on a feline brain (*left*) and the evoked response from each electrode (*right*) (adapted with permission from Reference 88; copyright 2010 Springer Nature). (*e*) Illustration of a pressure sensor with microhairs for conformal contact on the human skin measuring artery pulse waves (adapted with permission from Reference 94; copyright 2015 Wiley-VCH). (*f*) Illustration (*left*) and SEM image (*right*) of electrically conductive electrodes with mushroom-shaped micropillars for conformal contact and enhanced adhesion strength (adapted with permission from Reference 95; copyright 2016 ACS). (*g*) Three-dimensional atomic force microscopy images (*left*) and magnified view (*right*) of a microcrater array, which achieved enhanced skin adhesion and conformability (adapted with permission from Reference 96; copyright 2016 Wiley-VCH). (*h*) Optical image of a finger tube with transfer-printed and flipped stretchable electrodes for fingertip electrotactile stimulation (adapted with permission from Reference 97; copyright 2012 IOP Publishing). (*i*) Optical image of a 3D multifunctional integumentary membrane integrated on a rabbit heart (*bottom*) and the corresponding graphical depiction of device design and fabrication (*top*) (adapted with permission from Reference 98; copyright 2014 Springer Nature). (*j*) Photograph of an epicardial mesh implanted in a rat heart (adapted with permission from Reference 99; copyright 2016 AAAS). (*k*) Optical image of the high-density curved image sensor array with a soccer ball–inspired truncated icosahedron design. Inset shows the image captured by the sensor (adapted with permission from Reference 100; copyright 2017 Springer Nature). Abbreviations: CurvIS, curved image; ECG, electrocardiogram; GET, graphene electronic tattoo; ILED, inorganic light-emitting diode; SEM, scanning electron microscopy.

The same theory has guided the design of fully conformable graphene e-tattoo (GET), shown in **Figure 4*c*** (87). Because the mechanical property of the GET is dominated by the polymethyl methacrylate substrate, a plane strain modulus of 3.3 GPa was adopted for the GET. The model predicts that GET thickness should not exceed 510 nm to achieve full conformability to human skin. Indeed, the final GET with a thickness of 463 ± 30 nm could fully conform to the texture of natural skin. Thanks to the conformal contact, the GET–skin contact impedance was on par with that of gel electrodes, and the signal-to-noise ratio (SNR) of the dry GET (15.22 dB) was higher than that of the wet Ag/AgCl gel electrode (11 dB).

The same model is also applicable to wet interfaces of implantable devices with interface adhesion higher than water surface tension, i.e., 144 mJ/m^2. Consider polyimide-dominant electrodes laminating on a feline brain in vivo with a modulus of 50 kPa, wavelength of 11.86 mm, and amplitude of 0.24 mm, as shown in **Figure 4*d*** (88). The model predicts conformability thinner than 5 μm and device thickness of 2.5 μm. Experimentally, conformability with feline brain tissue was achieved with electrodes. The 28-channel electrode array recorded evoked potential response on the feline brain with a mean rms amplitude ratio of 5.7 and an excellent uniformity across the array.

In addition to making the device thinner and softer, another effective way to enhance conformability is to improve adhesion at the device–tissue interface. Both chemical and physical routes have been explored for this purpose, but here, we focus only on adhesion enhanced through structural designs. The groundbreaking discovery of microfibrils on gecko toe pads (89) has opened up the field of dry adhesives (90, 91). The mechanics of how microfibrils enhance van der Waals adhesion has been well investigated (92, 93). By adding an array of polydimethylsiloxane (PDMS) micropillars with an aspect ratio of 10, Pang et al. (94) improved the contact between a soft pressure sensor and pigskin from 25% to 98% (**Figure 4*e***). As a result, the pressure sensor showed 12 times higher SNR than that without micropillars, which enabled the measurement of extremely weak signals from jugular venous pulses. Kim et al. (95) designed electrically conductive, mushroom-shaped micropillars to achieve a normal adhesion strength of ∼1.3 N/cm^2 on rough human skin, as well as a reusability of 30 times (**Figure 4*f***). This conformable electrode has been applied successfully to measure ECG signals on both dry and wet skin. An octopus-inspired microcrater array

has also been explored for dry adhesives. Choi et al. (96) manufactured smart medical skin with microsurface craters with rims mimicking those of cephalopod suckers (**Figure 4*g***). It achieved an almost threefold increase of normal adhesive strength, and the adhesion did not degrade after 50 h or 8 reuses. This smart medical skin could fully conform to human skin and successfully measure biometrics such as ECG and pulse waveforms. The mechanics of surface-crater-enabled dry adhesives remains elusive, but we review some preliminary studies based on idealized assumptions.

In addition to conforming to rough surfaces, soft bioelectronics also must conformly wrap around the overall 3D shape of the organ, such as a finger, heart, or retina. However, microfabricated bioelectronics begins to be planar. To overcome the 2D–3D mismatch, novel 3D conformability strategies have been developed. The first strategy is to directly model a 3D elastomeric sheath out of the 3D model of the organ, transfer-print a stretchable array of devices in a planar manner, let the sheath recover its 3D shape, and finally flip the 3D sheath outside-in, such that the electrodes can achieve direct contact with the tissue when put on. Examples include a finger tube for fingertip electro-tactile stimulation (97) (**Figure 4*h***) and a heart sock for spatiotemporal cardiac sensing and stimulation across the entire epicardium (98) (**Figure 4*i***). The second strategy is to engineer a highly stretchable planar open mesh. When wrapped around the heart, the elastoconductive epicardial mesh would stretch nonuniformly according to the 3D shape of the heart to achieve full conformability to the heart surface for both sensing and pacing (99) (**Figure 4*j***). Finally, to make a high-density, nonstretchable optoelectronic image sensor array conform to a hemispherical retina, Choi et al. (100) proposed a soccer-ball-inspired truncated icosahedron design to minimize device layer buckling and distortion after conformation (**Figure 4*k***).

2.3. Designed Deployability

Sometimes conformable devices on the tissue surface are insufficient to capture activities deep inside the organ/tissue, such as the heart, the nerve, and even the brain. In these cases, soft bioelectronics that can achieve 3D volumetric integration with the tissue without causing scars or immune responses are desirable. However, shifting from as-fabricated 2D electronics to 3D volumetric architecture poses a limited design challenge. We review recent emerging designs for deployable bioelectronics.

Endocardial surfaces are traditionally difficult to access. Single-lead catheters could perform point-by-point ablation to treat arrhythmia but with little sensing feedback. As a result, an inflatable, multifunctional balloon catheter has been engineered with stretchable electrodes, temperature sensors, and light-emitting diodes (LEDs), all in island-plus-serpentine designs, to perfectly wrap around a commercially available catheter balloon skin, which is cylindrical when deflated (101) (**Figure 5*a***). The catheter could easily meander through the blood vessels with small initial diameters. After reaching the right atrium of a porcine heart, the balloon was deployed with a hoop strain of 130% along the equator to make good contact with the endocardial wall. It could then measure contacting force and perform electrocardial mapping, radio frequency (RF), and ablation with in situ temperature mapping inside a beating heart. In addition to forced deployment owing to fluid injection, active materials have been incorporated to build stimuli-responsive smart deployable bioelectronics. For instance, Zhang et al. (102) used highly stretchable (∼1,100%), low-modulus (∼300 kPa), and biocompatible shape-memory polymer film to support a stretchable filamentary serpentine network of gold electrodes. This smart electrode was programmed to climb along the vagus nerve of a rabbit in a spiral, vine-like manner when subjected to body temperature (∼37°C) (**Figure 5*b***). The grabbing force enabled intimate contact between the electrodes and the vagus nerve, which ensured high-quality ECG recording, as well as electrical stimulations for a decrease in heart rate.

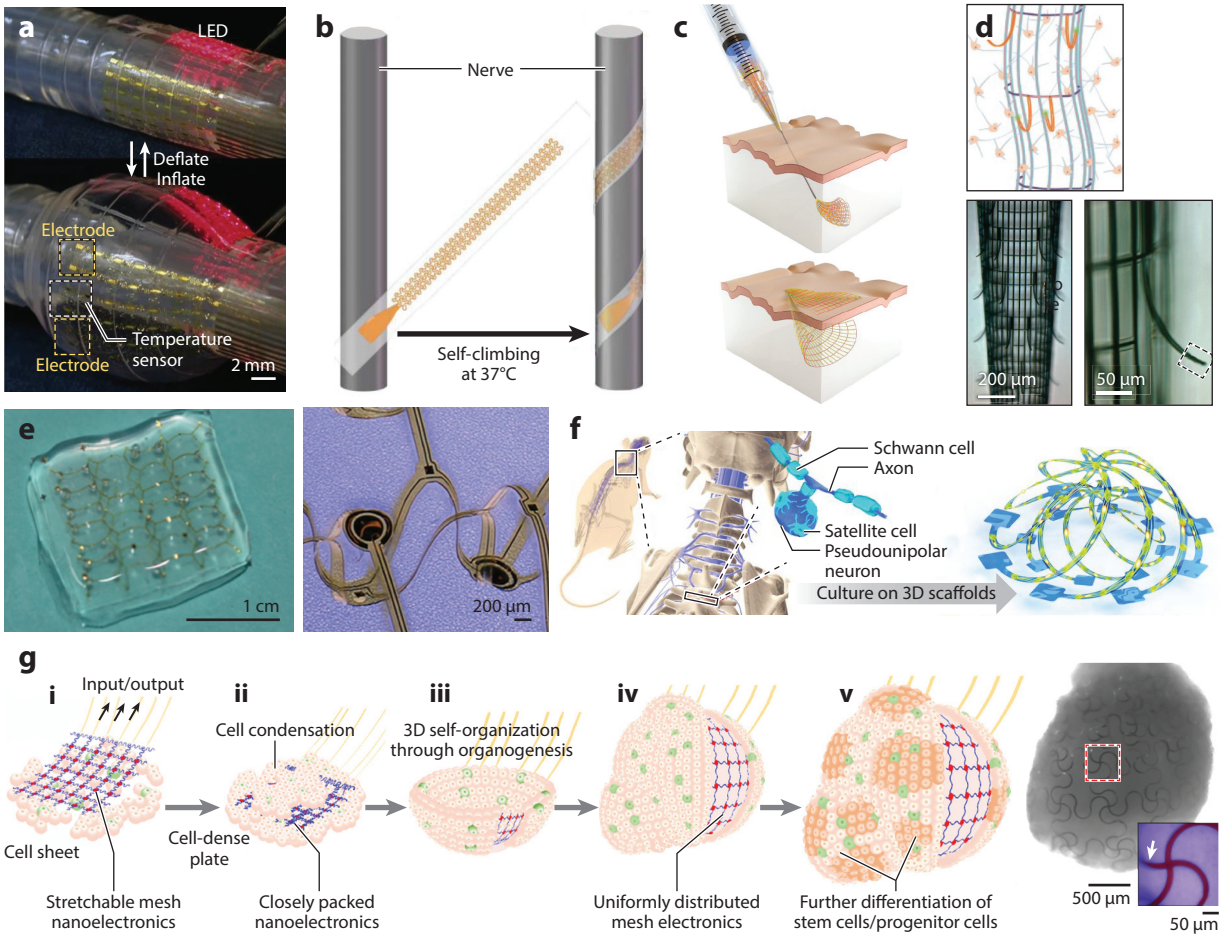

Figure 5

Device design for 3D deployability. (*a*) Optical images of a multifunctional balloon catheter in deflated (*top*) and inflated (*bottom*) states (adapted with permission from Reference 101; copyright 2011 Springer Nature). (*b*) Shape-memory polymer–based self-climbing electrodes under body temperature for nerve monitoring and stimulation (adapted with permission from Reference 102; copyright 2019 AAAS). (*c*) Illustration of syringe-injectable deep-brain monitoring electronics (adapted with permission from Reference 103; copyright 2015 Springer Nature). (*d*) Schematic of a porous cylindrical nanoelectronic brain probe (*top*) and micrographs of the self-organizing probe with outward bent arms as deployed microprobe (*bottom*) (adapted with permission from Reference 107; copyright 2015 Springer Nature). (*e*) Optical image of a freestanding 3D electronic scaffold integrated within an extracellular matrix hydrogel (*left*) and magnified image of the pop-up scaffold (*right*) (adapted with permission from Reference 110; copyright 2020 Elsevier). (*f*) Schematic illustration of rat dorsal root ganglion neural networks and the cell populations within them (*left*), as cultured on 3D pop-up electrodes (*right*) (adapted with permission from Reference 111; copyright 2017 NAS). (*g*) Schematic illustration (*left*) and optical image (*right*) of the integration process of stretchable mesh nanoelectronics into organoids through organogenesis. Inset shows a bright-field phase image of the resulting organoid (adapted with permission from Reference 112; copyright 2019 ACS). Abbreviation: LED, light-emitting diode.

There are approximately 86 billion neurons in the human brain. Deep-brain recording or stimulation with minimally invasive means calls for deployable electrodes for minimally invasive delivery but expanded volumetric recording. One pioneering method involves syringe-injectable electronics (103–105) (**Figure 5*c***). Silicon nanowire transistors and metal electrodes on an ultrathin epoxy layer (300–400 nm) were patterned into an open mesh layout. The device was folded

and crumpled to fit inside a syringe, which could be easily inserted into the deep brain and then eject the device. After ejection from the syringe, the device could naturally deploy owing to mesh self-recovery, resulting in 3D coupling with neurons in the deep brain (106). In later work, Xie et al. (107) demonstrated a 3D-macroporous device, which could spontaneously curve into a cylindrical surface (**Figure 5*d***). On this porous cylinder, an array of microelectrode arms were able to bend outward inside the brain owing to nonuniform residual stresses in the arm layers, effectively enhancing the measuring volume. The modulated elasticity and high deformability enabled intimate contact between the device and brain tissue. Moreover, the macroporous structure allowed neurons to penetrate into the device. Five weeks after implantation, regenerated neural tissues fully encapsulated the 3D electrode without notable inflammatory reactions or vacancies, implying that high-quality, long-term contact had been achieved between the electrode and the neuron cells.

Another strategy to couple electronics and soft tissue in 3D is through cell growth. A 3D pop-up microelectronic structure could form in a deterministic fashion through the controlled mechanical buckling of the predesigned 2D precursor (108, 109). After embedding the 3D microelectronics in a hydrogel matrix, cardiac tissue cells could be cultivated into a 3D scaffold that was fully integrated with the 3D microelectronics (110) (**Figure 5*e***). The device could then perform sensing, stimulation, and regulation of tissue function during tissue growth. Owing to their thinness and softness, the pop-up electronics posed almost no effect on cardiac cell viability. In follow-up research, Yan et al. (111) fabricated freestanding 3D pop-up electrodes without elastomeric substrates to eliminate their constraints on operating temperatures and dimensional stability (**Figure 5*f***). The 3D bilayer–nested cages of epoxy were applied as growth platforms for neural networks of dorsal root ganglion cells dissociated from explants of rats. The cells were organized into networks following the 3D mesostructure and formed shortcuts between ribbons. By using the microelectrodes fabricated on the epoxy, the electrophysiological (EP) activities of the 3D growing neural cell networks could be monitored successfully.

The 2D-to-3D structural transition could even be induced directly via cell growth, which enabled so-called cyborg organoids (112) (**Figure 5*g***). First, planar nanoelectronics with an island-plus-serpentine open mesh design were laminated on the surface of a 2D sheet of stem cells. Attraction forces between cells during cell growth gradually shrank the cell sheet into a cell-dense plate, compressing the nanoelectronics into a closely packed architecture and embedding them within the cells. Owing to organogenesis-induced self-folding, the interwoven cell–nanoelectronic structure contracted, curled into a bowl, and finally closed up to form a 3D spherical shell. During the cell growth process, the mesh nanoelectronics seamlessly reconfigured with the cell plate owing to their negligible bending and tensile rigidity, while maintaining uniform spatial distributions throughout the tissue, leading to a fully grown 3D organoid with volumetrically well-distributed sensors and stimulators.

3. NOVEL MATERIALS FOR SOFT BIOELECTRONICS

Adopting the aforementioned device designs to reduce and/or redistribute the mechanical stress applied to the bioelectronics is a useful strategy to fabricate soft devices. However, the intrinsic characteristics of the rigid films, which are identical to those of biological tissues, remain unchanged. Therefore, local mechanical mismatches still exist. And thus, several novel materials have been introduced for soft bioelectronics, such as liquid metal, nanotubes and nanowires, conductive fabrics, conducting polymers, hydrogel composites, and elastomer nanocomposites, to mimic the mechanical and electrochemical characteristics of biological tissue (113). In this section, we present representative cases of such novel materials.

3.1. Liquid Metal

Liquid metal is highly conductive and is in its liquid state at room temperature. Owing to its fluidity, proper encapsulations of the material, such as the liquid metal in microfluidic channels, are essential for flexible and/or stretchable electrodes (**Figure 6*a***). Despite the complicated fabrication processes and leakage risks, it has been considered a promising option for the soft bioelectronics, because the devices fabricated with liquid metal show high stretchability as well as high conductivity.

For example, Guo & Liu (114) demonstrated an electrode of GaIn alloy (75.5% Ga and 24.5% In by weight fraction) encapsulated by a 250-μm-thick PDMS elastomer (**Figure 6*b***). The electrode showed soft mechanical properties (elastic modulus of 1.05 MPa), and the conductance of the GaIn alloy electrode was stable, with only a small resistance change (∼4 Ω) even after 7,000 cycles of stretching (applied strain of 15%). The GaIn liquid metal alloy was infiltrated through holes with a diameter of ∼1 mm to fill the PDMS channels and form long conducting interconnects. To assess biocompatibility, the cytotoxicity of the electrode was tested with mouse fibroblasts, and the high viability of fibroblast cells was obtained. By using the GaIn alloy electrode, Guo & Liu could stimulate the sciatic nerve of a bullfrog to make its lower limb move. This demonstration proved the potential use of liquid metal for stimulation electrodes.

Typically, a single liquid component has been used for liquid metal–based devices, because two liquids can be mixed at their junction. Ota et al. (115) developed a method to make a heterojunction between liquid metal and an ionic liquid. They fabricated a device using Galinstan (68.5% Ga, 21.5% In, 10% Sn) and an ionic liquid encapsulated in PDMS microchannels (30 μm wide, 31 μm high, and 200 μm long). An ionic liquid reservoir was sandwiched between two Galinstan reservoirs, connected by several microfluidic channels. The surface of the PDMS microchannels was plasma treated to control its surface energy. Such plasma treatment controlled the surface energy of PDMS and tuned the contact angle of Galinstan on PDMS to 134°. The balance between the surface energy and the external pressure allowed infiltration and prevented leakage of Galinstan. This heterojunction between two liquids was used as a sensor, in which Galinstan served as an electrode and the ionic liquid served as a sensing element to detect temperature, humidity, and oxygen concentrations. The heterojunction endured stretching up to the strain of 90% and twisting up to 60°.

Another property of liquid metal is that it can change its phase at a modest temperature. This phase-shifting property can be used to fabricate a rigidity-tunable neural implant. Wen et al. (116) fabricated a soft, intracortically implantable electrode made of gallium (Ga) and showed temperature-dependent control of its stiffness by using a solid-liquid phase transition of Ga. Ga can shift between liquid and solid phase around body temperature, which varies its stiffness over 5 orders of magnitude. This bioelectrode was inserted into a rat brain without a supporting shuttle. Once inserted into the brain in solid state, the probe became soft within a few minutes owing to its phase change into a liquid state.

Meanwhile, by using this phase transition property, the liquid metal can be processed into diverse shapes, including 3D architectures (117). Liquid-phase eutectic gallium-indium (EGaIn) was dispensed on a cold plate via a nozzle and instantly changed its phase to a solid state (**Figure 6*c***). After the 3D printing of EGaIn liquid metal, the frozen metal structure was encapsulated by an elastomer precursor. After the elastomer was fully crosslinked, the solid-state 3D EGaIn structure was melted back into a liquid state, which was encapsulated by the crosslinked elastomer. Highly conductive (∼34,000 S/cm) and complicated soft 3D structures could be demonstrated via this process, which can endure deformations (**Figure 6*d***).

Although liquid metal is soft and highly conductive, the application of liquid metal to soft bioelectronics has been somewhat limited, mainly because the liquid metal must be firmly entrapped

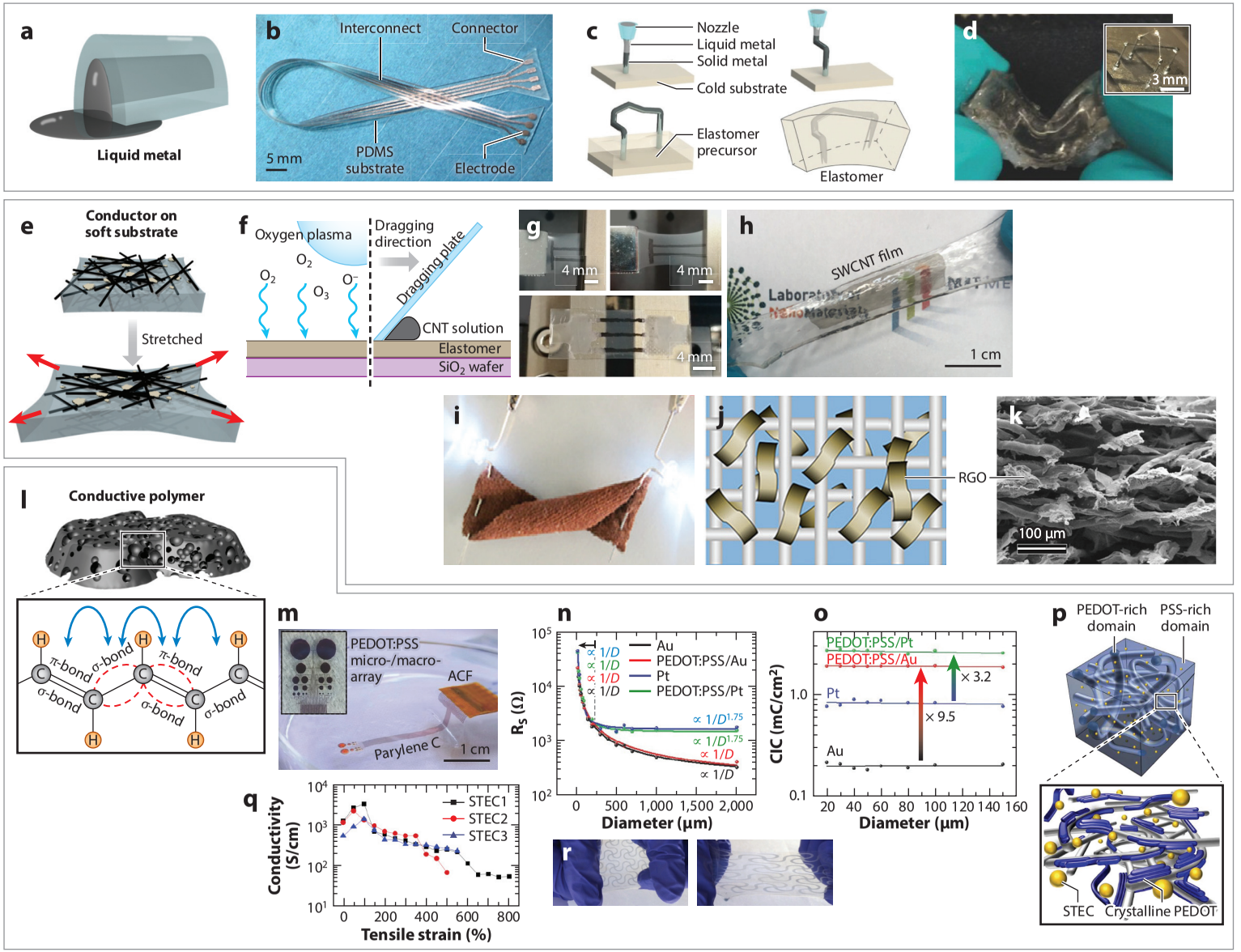

(Caption appears on following page)

Figure 6 (*Figure appears on preceding page*)

Novel materials for bioelectronics. (*a*) Schematic image of liquid metal embedded in the elastomeric channel. (*b*) GaIn liquid metal electronics encapsulated in PDMS elastomer (adapted with permission from Reference 114; copyright 2017 IOP Publishing). (*c*) Three-dimensional printing process of liquid metal. (*d*) Bending 3D structure encapsulated in elastomer. Inset image indicates the complex 3D structure. Panels *c*,*d* adapted with permission from Reference 117; copyright 2016 Wiley-VCH. (*e*) Schematic image of a conductive material coated on the soft substrate. (*f*) CNT coating process on the oxygen plasma–treated elastomeric surface. (*g*) CNT-patterned elastomer could be stretched to 100%. Panels *e*,*f* adapted with permission from Reference 122; copyright 2019 MDPI. (*h*) The stretchable SWCNT film coated on the hydrogel substrate (adapted with permission from Reference 123; copyright 2018 ACS). (*i*) Optical image presenting conductivity of the metal-coated fabric (adapted with permission from Reference 124; copyright 2018 ACS). (*j*) Schematic illustration and (*k*) SEM image of graphene oxide on a polymeric textile structure (adapted with permission from Reference 131; copyright 2017 ACS). (*l*) Schematic image of a conductive polymer. (*m*) Conductive polymer, PEDOT:PSS coated on the conventional flexible Au electrode. The inset image shows a magnified structure of the electrode (adapted with permission from Reference 133; copyright 2017 Wiley-VCH). (*n*) The impedance and (*o*) charge injection capacity of a bare metal electrode and PEDOT:PSS-coated metal electrode. Panels *n*,*o* adapted with permission from References 133, 134; copyright 2017 Wiley-VCH. (*p*) Schematic image of PEDOT:PSS structure with STEC enhancer. (*q*) Conductivity versus tensile stress curve of the STEC-enhanced PEDOT:PSS. (*r*) The STEC-enhanced PEDOT:PSS electrode could be stretched to be 600%. Panels *p*–*r* adapted with permission from Reference 136; copyright 2017 AAAS. Abbreviations: CNT, carbon nanotube; PAN, polyacrylonitrile; PDMS, polydimethylsiloxane; PEDOT, poly(3,4-ethylenedioxythiophene); PSS, polystyrene sulfonate; SEM, scanning electron microscopy; STEC, stretchability and electrical conductivity; SWCNT, single-walled carbon nanotube.

in elastomeric channels. Moreover, the liquid metal–based soft electronics feature a relatively thick device geometry because of the thickness of the elastomeric encapsulations for the liquid metal.

3.2. Conductive Nanomaterials Coated on Soft Substrates

A conductive nanomaterial network patterned on a stretchable substrate can be another candidate for soft bioelectronics (118, 119) (**Figure 6*e***). The percolated nanomaterial network provides electrical conduction pathways, whereas the elastomeric substrate provides stretchability (120). Conductive nanomaterials, such as carbon nanotubes (CNTs) (121) or metal nanowires, can be adhered on the elastomer via the surface treatment of both nanomaterials and elastomer substrates. The percolation network between individual nanomaterials can be maintained under stretching. For example, Lee et al. (122) patterned a thin (80–330-nm) CNT layer on an O_2-treated elastomer (a mixture of Ecoflex and PDMS) (**Figure 6*f***), which could endure >100% stretching (**Figure 6*g***).

In addition to elastomer substrates, hydrogels can also serve as soft substrates. Hydrogels typically exhibit a lower modulus and better compatibility with tissue than elastomers. For example, Gilshteyn et al. (123) fabricated a conductive, stretchable, and transparent wearable electrode by using a single-walled CNT (SWCNT) film coated on a tough hydrogel (**Figure 6*h***). First, an ultrathin (~40-nm) SWCNT film was deposited on the nitrocellulose filter and cut into the desired shape. Then, the patterned SWCNT film was pressed against the tough hydrogel, which transferred the film onto the tough hydrogel substrate. The SWCNT–hydrogel film showed a resistance of ~100 Ω/cm, a transparency of 80% (at 550 nm), and a stretchability of ~100%. These thin conductive films coated on soft substrates could serve as soft bioelectrodes.

As another form of soft substrate, woven fabrics have been applied to electrically conductive fabric, which is lightweight, breathable, flexible, and stretchable. Conductive materials, such as metal films (**Figure 6*i***) (124), carbon nanomaterials (125–127), metal nanomaterials (128), and conductive polymers (129, 130), have been coated on the fabrics. For example, silver nanowires (AgNWs) and polyurethane (PU) layers were coated on a carbon fiber fabric. First, the fabric, composed of bundles of carbon fibers, was coated with AgNWs. Then, a PU solution was dropped on the AgNW-coated fabric, followed by drying and curing of the PU solution. The PU layer prevented delamination of AgNWs from the fabric. The resultant conductive fabric showed a conductivity of 15,930 S/cm. The conductive fabric endured bending tests of 5,000 cycles with

a bending radius of 2.0 mm. As a demonstration, Song et al. (131) fabricated an electromagnetic interference shielding device with a thickness of 0.36 mm. The resultant shielding effect was 106.0 dB.

Another fabrication approach involves constructing a conductive fabric by weaving conductive fibers, instead of depositing conductive films on insulative fabrics. Zhao et al. (132) fabricated conductive fibers by coating polyacrylonitrile (PAN) fibers with Cu (**Figure 6*j***). A 300-nm-thick Cu film was coated on PAN fibers via the electroless deposition method, attaining a conductivity of ~0.15 Ω/cm. In addition to the Cu-coated conductive PAN fibers, parylene-coated insulative PAN fibers were also used to fabricate a conductive fabric via conventional textile manufacturing processes, such as stitching, weaving, and knitting (**Figure 6*k***). Fabric properties could be controlled, such as various air resistances (impermeability of air) of 0.085, 0.01, and 0.04 kPa·S/m and water vapor transmissions of 1,300, 1,250, and 1,200 g/m^2·day, depending on the fiber's weaving density. A triboelectric wearable pressure sensor could be demonstrated by using the conductive fabric.

3.3. Conductive Polymer

Conjugated conductive polymers consist of backbones with alternating double and single bonds. Electrons flow via repeating π-bonds throughout the conductive polymer chain and contact with surrounding electrolytic biofluids, which result in ion/electron exchanges. This property of conductive polymers is suitable for their interfacing to ion-rich tissues. Most conductive polymers are biocompatible in their polymeric state. Therefore, they have been used as electrodes or surface-coating materials for soft bioelectronics (**Figure 6*l***). Conductive polymers include polyaniline, polyterthiophene, polypyrrole, poly(ethylene dioxythiophene) (PEDOT), and their modifications.

Compared with conventional metals, conductive polymers show superb electrochemical performance, such as high charge injection limit, high charge injection capacity, and low impedance, which are important criteria for high-quality EP recording and stimulations. Ganji et al. (133, 134) compared the electrochemical properties of Au, Pt, and poly(3,4-ethylenedioxythiophene): polystyrene sulfonate (PEDOT:PSS) (**Figure 6*m***) with regard to ECoG recording. The PEDOT:PSS electrode showed higher faradaic charge transfer and capacitive charge coupling than the metal electrode, which resulted in lower impedance and higher SNR (134) (**Figure 6*n***). Specifically, the charge injection capacity of PEDOT:PSS on a Pt electrode was 2.71 mC/cm^2, 3.2 times higher than that of the bare Pt electrode (0.83 mC/cm^2). Also, the charge injection capacity of PEDOT:PSS on a Au electrode was 1.9 mC/cm^2, 9.5 times higher than that of the bare Au electrode (0.2 mC/cm^2) (133) (**Figure 6*o***). The PEDOT:PSS coating was effective only on the electrode smaller than 200 μm in diameter, because the effect of resistance is dominant for electrodes larger than 200 μm in diameter. Ganji et al. (135) recorded ECoG signals in vivo with the PEDOT:PSS-coated electrode on a human patient, which demonstrated high-quality neural recording and modulation under various clinical conditions.

To compensate for their low conductivity and stretchability, conductive polymers have been mixed with nanomaterials, hydrogels, or ionic liquids (136–138). **Figure 6*p*** describes a mixture of PEDOT:PSS with an additive that enhances stretchability and electrical conductivity (known as a STEC enhancer) (136). The STEC enhancer, which includes ionic compounds and ionic liquids, reinforced the stretchability and conductivity of the PEDOT:PSS mixture. STEC enhancers partially softened polymer chains to create soft domains in the polymer matrix and also connected PEDOT-rich domains to make a conductive network inside the soft PSS-rich domain. The film prepared with PEDOT:PSS and STEC enhancers exhibited a conductivity of >3,100 S/cm at 0% strain and a conductivity of >4,100 S/cm at 100% strain (**Figure 6*q***). Also, the conductivity

could be maintained at 3,600 S/cm even after 1,000 cycles of stretching (100% strain). The film was conductive (above 100 S/cm) even under 600% strain. The material could be patterned for fabricating devices with a complex geometry (**Figure 6*r***). Although they show remarkable electrochemical properties, conductive polymers themselves still suffer from low conductivity and a high Young's modulus. Therefore, appropriate additives are important.

3.4. Conductive Hydrogel Composites

Excellent mechanical properties similar to those of tissues, high water content, and ionic permeability within the crosslinked polymeric network render hydrogels attractive material candidates for soft bioelectronics (139). Conductive filler materials can be introduced to a hydrogel matrix, leading to conductive hydrogel composites (140, 141) (**Figure 7*a***). In addition to the ion-rich property of hydrogels, the percolation network of conductive fillers in the hydrogel matrix contributes to high conductivity, low impedance, and high charge injection capacity (142).

Despite such advantageous material properties, hydrogel composites' high-resolution patterning poses a challenge for device fabrication. Hydrogels' porous, water-rich properties are not compatible with conventional photolithography and dry etching processes. Thus, Liu et al. (143) developed a method to apply photolithography and etching to the patterning of a conductive hydrogel. First, the PEDOT:PSS-ionic liquid (PEDOT:PSS-IL) ion gel was patterned via the conventional photolithography and dry etching process. Then, the micropatterned PEDOT:PSS-IL was transformed into a conductive hydrogel via water exchange. The micropatterned electrically conductive hydrogel (MECH) exhibited a resolution of <5 μm (**Figure 7*b***). Additionally, fluorinated elastic photoresist using dimethacrylate-functionalized perfluoropolyesther was used as an insulating layer for the MECH electrode. The freestanding MECH electronics showed 20% stretching without cracks (over 10,000 stretching cycles) and high softness (a modulus of ∼30 kPa). As expected, MECH showed a high charge storage capacity (CSC) of 164 mC/cm^2, much higher than that of PEDOT (75.6 mC/cm^2), platinum (0.55 mC/cm^2), or IrOx (28.8 mC/cm^2). Also, the fully patterned MECH electrode exhibited 10 times and 20 times lower impedance than the hydrogel coated on the Au electrode and silane-crosslinked PEDOT:PSS on Au electrode, respectively (**Figure 7*c***). Moreover, Liu et al. demonstrated low-voltage electrical stimulations on sciatic nerves of mice for two months by using the MECH electrode.

Homogeneous dispersion of the filler material in the hydrogel matrix is critical for the mechanical and electrical properties of the composite. PEDOT:PSS nanofibril hydrogels were developed by mixing dimethyl sulfoxide with an aqueous PEDOT:PSS solution, followed by dry-annealing and rehydration (138). With an optimized dimethyl sulfoxide content (13 vol.%), the hydrogel exhibited high electrical conductivity (∼40 S/cm in deionized water), high stretchability (>35% strain), and a low Young's modulus (∼2 MPa) (**Figure 7*d***). Note that the hydrogel features swelling properties that are tunable depending on the dry-annealing condition, and thus the hydrogel can swell isotropically or anisotropically (**Figure 7*d***, *inset*).

Conductive filler nanomaterials other than PEDOT:PSS, such as carbon and metal nanomaterials, have been applied to fabricate conductive hydrogel composites. In terms of affinity between filler materials and hydrogels, carbon nanomaterials are more compatible than metal nanomaterials. Graphene (144), CNT, and their derivatives are promising filler materials for hydrogel composites. For example, conductive hydrogels fabricated with polyvinyl alcohol-borax hydrogel, TOCNFs (2,2,6,6-tetramethylpiperidine-1-oxyl-cellulose nanofibers), CNTs, and polyaniline showed reasonable mechanical (modulus of ∼18.2 kPa) and electrical (15.3 S/m in conductivity and 226.8 F/g in specific capacitance) performance (142). In this material, TOCNF serves as a dispersant of CNTs in the hydrogel matrix. Polyaniline enhances electrochemical performance,

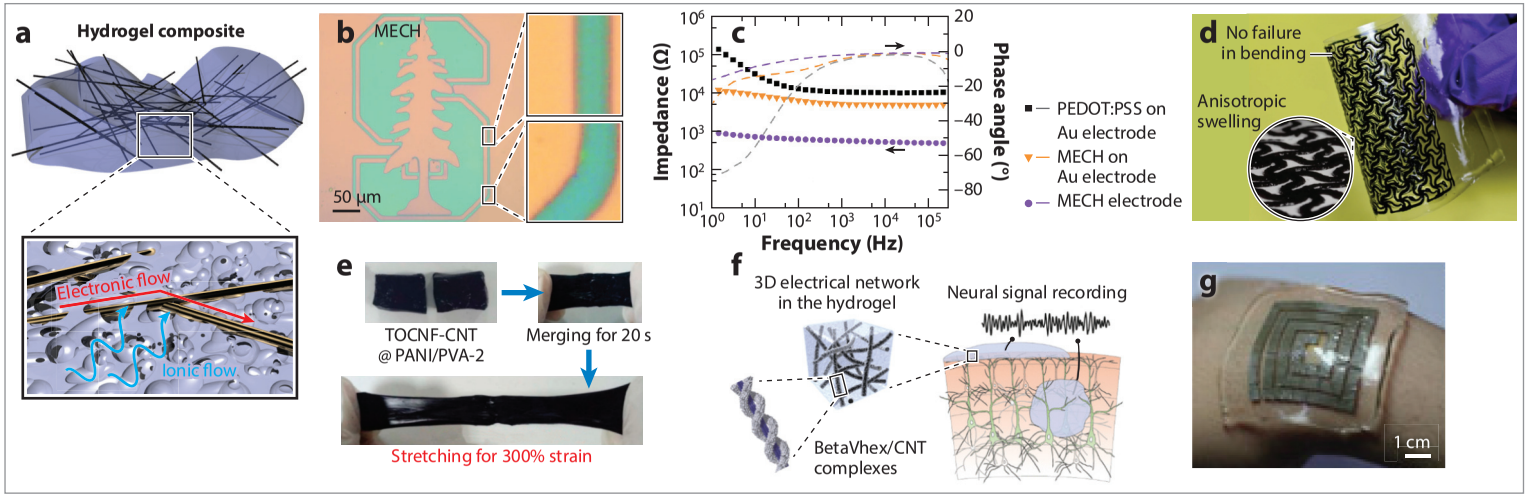

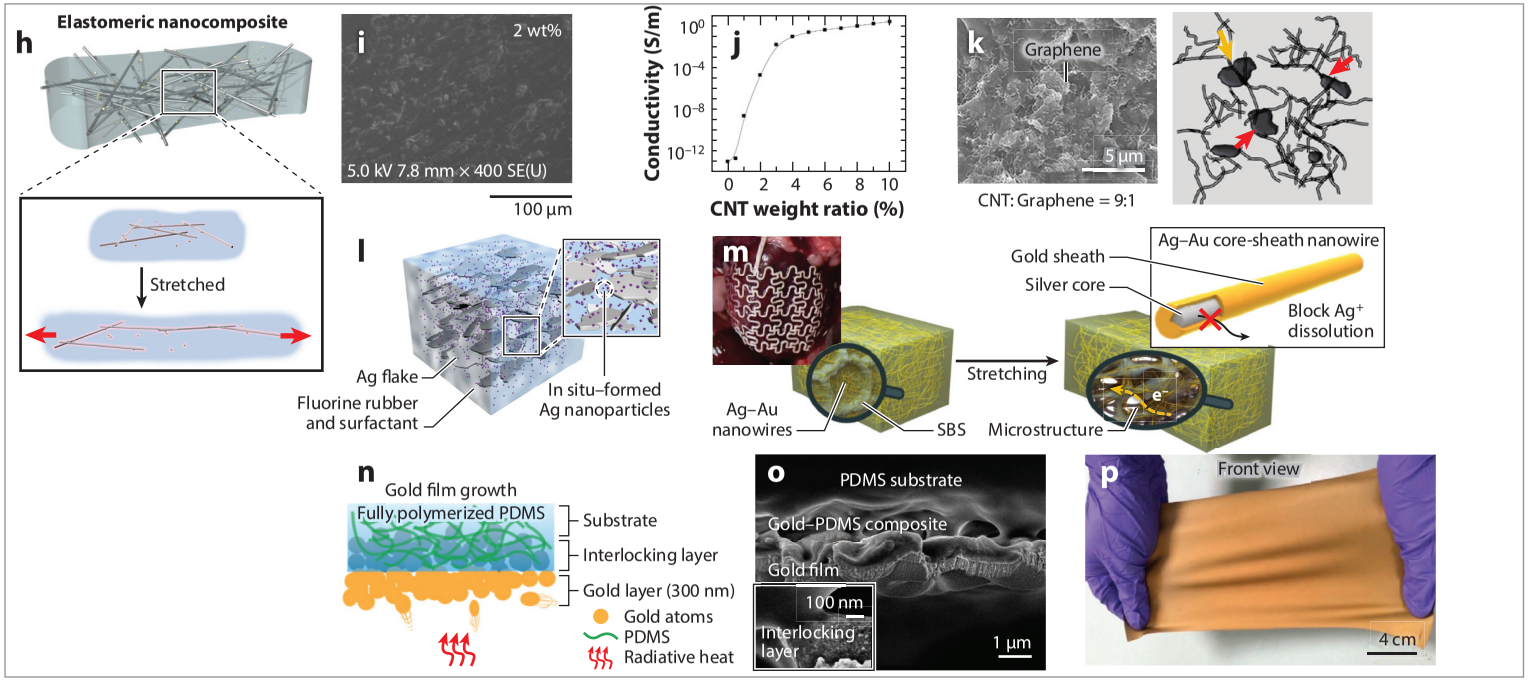

(Caption appears on following page)

Figure 7 (*Figure appears on preceding page*)

(*a*) Schematic illustration of a hydrogel and composite. (*b*) Photolithography-patterned MECH electronics and its magnified images. (*c*) The impedance of the MECH electrode, hydrogel coated on Au electrode, and PEDOT:PSS coated on Au electrode. Panels *b*,*c* adapted with permission from Reference 143; copyright 2019 Springer Nature. (*d*) Optical image of PEDOT:PSS nanofibril hydrogel composite electronics, developed by DMSO (adapted with permission from Reference 138; copyright 2019 Springer Nature). (*e*) Self-healable, stretchable hydrogel composite composed of hydrogel, nanofibers, CNTs, and PANI (adapted with permission from Reference 142; copyright 2020 MDPI). (*f*) BetaVhex/CNT hydrogel composite, which can be implanted in the animal cortex (adapted with permission from Reference 145; copyright 2020 ACS Publications). (*g*) Wearable antenna made of alginate-AgNW nanocomposite (adapted with permission from Reference 146; copyright 2018 AIP Publishing LLC). (*h*) Schematic illustration of the elastomeric nanocomposite. (*i*) SEM image of CNT–PDMS nanocomposite. (*j*) Conductivity versus CNT weight ratio curve of CNT–PDMS nanocomposite. Panels *i*,*j* adapted with permission from Reference 149; copyright 2020 MDPI. (*k*) CNT-graphene dual-filler composite in PDMS matrix (adapted with permission from Reference 95; copyright 2016 ACS Publications). (*l*) Elastomeric nanocomposite composed of Ag flakes and fluorine rubber. Ag nanoparticles are formed in the matrix in situ (adapted with permission from Reference 157; copyright 2017 Springer Nature). (*m*) Metallic nanowires are dispersed in SBS elastomeric matrix and can be stretched with microstructure. The elastomeric nanocomposite could be wrapped on the heart surface (*left inset*) (adapted with permission from Reference 99; copyright 2016 AAAS). The Au sheath coated on the AgNW to enhance biocompatibility (*right inset*) (adapted with permission from Reference 158; copyright 2018 Springer Nature). (*n*) Schematic illustration explaining the mechanism of Au atom doping in the PDMS matrix. (*o*) SEM image of Au-doped elastomer. (*p*) The Au-doped elastomeric composite could be stretched to 130%. Panels *n*–*p* adapted with permission from Reference 160; copyright 2019 Wiley-VCH. Abbreviations: AgNW, silver nanowire; CNT, carbon nanotube; DMSO, dimethyl sulfoxide; MECH, micropatterned electrically conductive hydrogel; PANI, polyaniline; PDMS, polydimethylsiloxane; PEDOT, poly(3,4-ethylenedioxythiophene); PSS, polystyrene sulfonate; SBS, styrene-butadiene-styrene; SEM, scanning electron microscopy; TOCNF, 2,2,6,6-tetramethylpiperidine-1-oxyl-cellulose nanofibers.

whereas CNTs contribute to conductivity. The conductive hydrogel endured 400% stretching and exhibited self-healing ability (**Figure 7*e***).

In another example, Nam et al. (145) proposed a 3D conductive network of CNTs complexed with proteins. The authors fabricated a neural interfacing device with a hydrogel based on the supramolecular β-peptide. The β-peptide (betaVhex) assembled with CNTs to form biocompatible and conductive electrical percolation networks (betaVhex/CNT complex) inside the hydrogel matrix. The betaVhex/CNT hydrogel nanocomposite (1% w/v betaVhex/CNT hydrogel) presented a modulus of ∼1,500 Pa and conductivity of 0.1345 S/m. It could be implanted in the intracortical area via syringe injection (**Figure 7*f***). The betaVhex/CNT hydrogel nanocomposite could form a tight contact with the neural tissue owing to its soft mechanical property. The injectable hydrogel nanocomposite was implanted in the somatosensory cortex of an epileptic mouse model and recorded the local field potential of epileptic events.

Highly conductive metallic nanomaterials can also be applied to the conductive hydrogel composite as a conductive filler material. Recently, Lim et al. (146) presented a composite of AgNWs embedded in an alginate hydrogel. Because the alginate hydrogel does not require covalent bond formation, crosslinking was possible in the presence of AgNWs. The alginate hydrogel–based composite was prepared by drying the hydrogel–AgNW solution, and the composite film was patterned via a laser-cutting process. The AgNW–alginate hydrogel composite showed a Young's modulus of 15.5 MPa and could be stretched up to 30%. The impedance of the nanocomposite with 0.5% filler content was extremely low (∼8.5 Ω) for all frequency ranges (10^0∼10^5 Hz). The resulting nanocomposite was applicable to various wearable devices, such as a wearable antenna (**Figure 7*g***) or supercapacitor.

Conductive hydrogel composites show extraordinary mechanical and biological compatibility with tissue and superb biochemical properties, which are important for soft wearable/implantable bioelectronics. However, relatively poor processability (owing to swelling properties and high moisture content) and low electrical conductivity impede their widespread application to electronic devices. Further development of novel materials and fabrication techniques could solve these issues.

3.5. Elastomeric Nanocomposites

Recently, elastomeric nanocomposites fabricated by embedding conductive nanomaterials in elastomers have been developed (113). They feature high stretchability and conductivity. The conductive nanomaterials form a 3D conductive percolation network in the elastomeric matrix (**Figure 7*b***). This percolation network is maintained and/or rearranged during the mechanical deformation of the nanocomposite. Various conductive nanomaterials, such as graphene flakes, CNTs (147), metal nanoparticles, and metal nanowires (148), have been studied as nanocomposite filler materials.

Carbon-based nanomaterials, including carbon blacks, CNTs, and graphene flakes, have been used as fillers for conductive nanocomposites owing to their deformable mechanical properties, electrical conductivity, and facile chemical functionalizations. Owing to their large aspect ratio, 1D CNTs efficiently form a percolation network in an elastomer. For example, CNT-PDMS nanocomposites have been applied to soft bioelectronics (149–155) (**Figure 7*i***). CNTs dispersed in PDMS show percolation thresholds of 2–4% (weight ratio of CNTs). The composite's conductivity increased with the ratio of CNTs, for example, 3×10^{-5} S/m at 2 wt%, 0.015 S/m at 3 wt%, 0.38 S/m at 6 wt%, and 2.3 S/m at 10 wt% (149) (**Figure 7*j***). As the CNT ratio increased, the Young's modulus also increased, from 3.4 MPa (pure PDMS) to 10 MPa (10 wt% CNTs in PDMS). Finding the optimal CNT content is necessary to balance nanocomposite conductivity and softness.

Although CNT nanocomposites show moderate conductivity, further improvement of conductivity is still required. In general, CNTs with better dispersion enable higher CNT composite conductivity, because they form an electrical percolation network at lower concentrations. Ultrasonication is generally employed for better dispersion of CNTs (156). Kim et al. (95) also proposed a nanocomposite with multiple types of carbon nanomaterials, such as graphene nanoflakes and CNTs (**Figure 7*k***). The composite of graphene flakes and CNTs in PDMS showed a stretchability of 100% and a resistivity of ∼100 Ω·cm. Note that conductivity was enhanced by ∼33% in comparison with the composite with CNTs only. A small amount of 2D carbon fillers (i.e., graphene flakes) played a key role. However, if the ratio of 2D carbon fillers to CNTs is higher than the optimized ratio, the synergetic effect disappears.

Metal nanomaterials, such as nanoparticles, nanoflakes, and nanowires, exhibit the highest conductivity among various fillers and thus could enable high-performance conductive nanocomposites. In nanocomposites, maintaining the percolation network of conductive fillers even under mechanical deformation is important for high conductivity as well as high stretchability. Several strategies to secure high-density percolation networks have been presented, such as the use of two filler components, high–aspect ratio fillers, and welding methods.

For example, Matsuhisa et al. (157) reported an elastic conductive nanocomposite containing two kinds of conductive fillers [Ag nanoparticles (nm-scale) and Ag flakes (μm-scale)] in fluorine rubber with a surfactant (**Figure 7*l***). Ag nanoparticles were synthesized in the composite in situ. The nanocomposite exhibited a conductivity of >4,000 S/cm at 0% strain and 935 S/cm at 400% strain. The nanoparticles could be rearranged under mechanical strain, forming conductive paths to compensate for broken percolation networks of Ag flakes. The nanocomposite could be printed on a textile, to be used as a wearable pressure and temperature sensor.

Nanomaterials with high aspect ratios have low percolation thresholds, which lead to high nanocomposite conductivity. Park et al. (99) developed a nanocomposite made of ultralong AgNWs and a poly(styrene-butadiene-styrene) elastomer. The nanocomposite showed a high conductivity of 11,210 S/cm. The authors used the stretchable conductive nanocomposite to fabricate a mesh-type electrode array, which could be wrapped around the heart (**Figure 7*m***,

left inset). In addition to the soft nature of the composite, the highly fractalized, hyperserpentine design resulted in high device elasticity (elastic modulus of 3.39 ± 0.849 kPa), which is lower than that of 2-mm-thick cardiac muscle (elastic modulus of 34.67 ± 6.2 kPa). Because the cardiac mesh showed mechanical properties similar to those of cardiac muscle, it could make excellent contact with the beating heart without impeding the heart's original systolic/diastolic motion.

In work by Choi et al. (158), AgNWs' cytotoxicity was reduced by capping nanowires with a thick gold sheath (Au@AgNW), thus preventing Ag oxidation and dissolution and guaranteeing biocompatibility and oxidation resistance of nanowires in vivo (**Figure 7*m*** and its right inset). Histology analyses revealed no notable cytotoxic and/or inflammatory reactions. Nanowire geometry (e.g., length, diameter) and weight fraction affect conductivity and stretchability. Sunwoo et al. (159) reported that adding platinum black (Pt black) to a Au@AgNW nanocomposite further improved electrical performance. The Au@AgNW–Pt black nanocomposite showed 3.3 times higher (~25 mC/cm^2) CSC and 8.4 times higher (0.61~5.12 mC/cm^2) charge injection limit than Au@AgNW alone. Use of the nanocomposite enabled high-quality ECG recording and effective cardiac resynchronization treatment in vivo.

Another strategy for incorporating metal atoms into elastomers was presented recently. Liu et al. (160) doped gold nanoparticles into an elastomer, depositing gold on partially cured PDMS via the thermal radiation–assisted metal deposition method (**Figure 7*n***). First, gold atoms bombarded and penetrated into semipolymerized PDMS, and the subsequent curing of PDMS completed fabrication of the conductive composite. During the curing, the modulus mismatch between gold and PDMS induced randomly wrinkled morphology on the film surface (**Figure 7*o***). This increased the effective surface area of the electrode by a factor of 5. This wrinkled surface contributed to low impedance. The resultant electrode had a stretchability of 130% and maintained a conductivity of >1 MS/m under 10,000 cyclic stretching tests (60% applied strain) (**Figure 7*p***). The electrode was implanted in rats to record intramuscular electromyogram (EMG) signals in vivo over four months.

Despite the high performance, i.e., high conductivity and high stretchability, of elastomeric nanocomposites, challenges remain. The elastomer's dense structure blocks penetration of ions and fluids, leading to poor electrochemical properties. The hydrophobic nature of many elastomeric nanocomposites shows their low cellular affinity compared with hydrogels. **Supplemental Table 1** summarizes the mechanical and electrochemical properties of each material introduced here. Each material has notable pros and cons (**Supplemental Table 2**), and appropriate materials can be chosen based on the intended application.

Supplemental Material >

4. SURFACE TREATMENT TO ENHANCE BIOCOMPATIBILITY

Several surface modification strategies have been used to improve the electrochemical properties and biocompatibility of soft bioelectronics. Most of the surface modification strategies have been applied to implantable bioelectronics. Such strategies are usually used to enhance bioelectronic performance. However, some surface modifications can also provide specific functions, such as delivery of chemicals and/or cells. In this section, we review strategies for surface modification using nanostructures and bioactive material coatings.

4.1. Surface Modification Using Nanostructures

Nanometer-scale bioelectronics can maximize surface area and thus increase interaction with the 3D microenvironment of the extracellular matrix (**Figure 8*a***). The high surface area also improves electrode performance, such as low impedance, high CSC, and high charge injection limit.

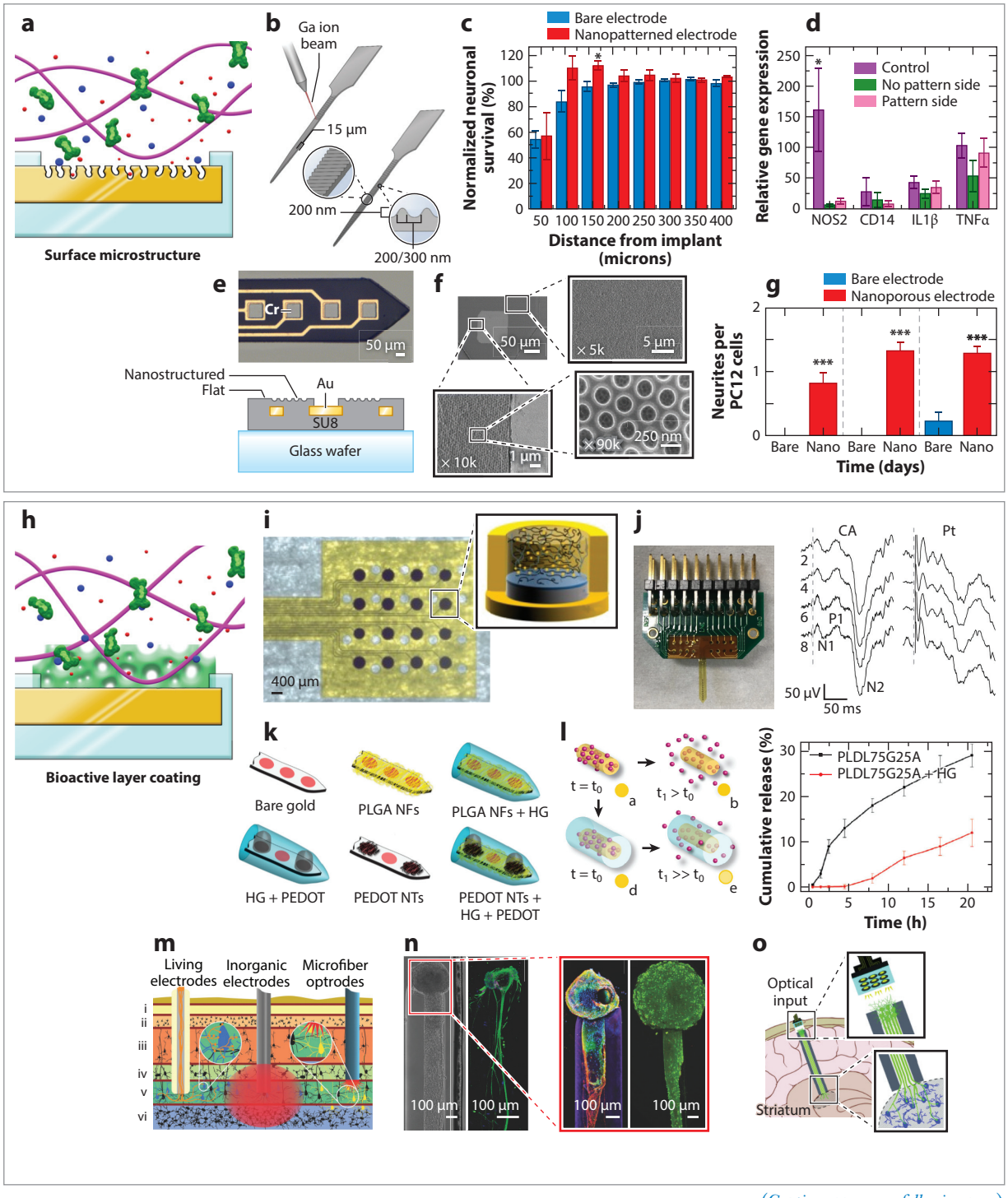

(*Caption appears on following page*)

Figure 8 (*Figure appears on preceding page*)

Surface treatment strategies to improve biocompatibility. (*a*) Schematic illustration of microstructure patterned on the electrode surface. (*b*) Schematic image of a nanopatterning process. (*c*) Neuronal survival rate of the bare electrode (*blue*) and nanopatterned electrode (*red*) depends on the distance from the implant. (*d*) Real-time polymerase chain reaction result of the nanopatterned and bare electrodes. Panels *b–d* adapted with permission from Reference 161; copyright 2019 Wiley-VCH. (*e*) Microscope image of an ultrathin Au electrode surrounded by a nanoporous epoxy substrate (*top*) and its structural view (*bottom*). (*f*) Scanning electron microscopy image of nanoholes. (*g*) Timescale graph of the number of PC12 cell survival on bare and nanoporous electrodes. Panels *e–g* adapted with permission from Reference 163; copyright 2017 Springer Nature. (*h*) Schematic illustration of a bioactive material coating on a bare electrode. (*i*) Optical image (*left*) and schematic illustration (*right*) of hydrogel coated on the flexible platinum electrode. (*j*) Optical image of fully packaged microelectrode array (*left*) and recorded visually evoked cortical potential from animal experiments (*right*). Panels *i,j* adapted with permission from Reference 164; copyright 2018 Frontiers Media S.A. (*k*) Complexed bioactive material, including NFs, PEDOT:PSS, hydrogel, and an anti-inflammatory drug, coated on a Au electrode. (*l*) The release mechanism (*left*) and profile (*right*) of an anti-inflammatory drug. Panels *k,l* adapted with permission from Reference 165; copyright 2009 Wiley-VCH. (*m*) Schematic image comparing living electrodes, inorganic electrodes, and microfiber optrodes. (*n*) Optical image and confocal reconstructed image of the living electrode. Red box indicates the magnified image. (*o*) Conceptual illustration of an implantable long axonal living electrode application in the deep brain. Panels *m–o* adapted with permission from Reference 171; copyright 2017 Wiley-VCH. Abbreviations: HG, hydrogel; NF, nanofiber; NT, nanotube; PEDOT, poly(3,4-ethylenedioxythiophene); PLGA, poly(lactic-*co*-glycolic acid); PSS, polystyrene sulfonate.

Ereifej et al. (161) fabricated a Michigan-style microelectrode with nanopatterned grooves on the surface to explore neuroinflammatory response in the rat cortex. The surface of the silicon intracortical microelectrode was etched by a focused ion beam to fabricate parallel grooves on the microelectrode (**Figure 8*b***). The pattern grooves have a width of 200 nm, a spacing of 300 nm, and a depth of 200 nm. In 4 weeks after implantation into the rat cortex, the electrode with a smooth surface and that with a nanopatterned surface were compared. Within a distance of 100–150 μm from the electrode, which is short enough to record single-neuron activity (50–140 μm), more neurons were observed in the case of the nanopatterned electrode than the control case ($p < 0.05$) (162) (**Figure 8*c***). Furthermore, real-time polymerase chain reaction data showed that the nanopattern could reduce inflammation-related gene expression (*HMGB1*, *NOS2*, and *CD14*) (**Figure 8*d***).

Similarly, Kim et al. (163) fabricated a porous structure for surface modification, demonstrating an implantable electrode consisting of ultrathin Au electrodes surrounded by nanoporous SU-8 epoxy. The ultrathin Au electrode was encapsulated with SU-8 epoxy (**Figure 8*e***, *top*), followed by patterning of the nanoporous structure via nanosphere lithography (**Figure 8*e***, *bottom*). The nanoholes had a diameter and depth of ∼200 nm (**Figure 8*f***). In vivo studies exhibited that neurons preferred the nanoporous structure, which resulted in a greater number of neurites than the control, whereas glial cells avoided the nanoporous structure. The nanoporous structure played an important role in neurite growth and served as a precursor of neuron dendritic spines. According to the culture result of PC12 cells on the bare and nanoporous structure for 5 days, PC12 cells proliferated and differentiated on the nanoporous structure but not on the bare surface (**Figure 8*g***), proving the enhanced biocompatibility of the electrode with the modified surface.

4.2. Surface Treatment by Coating Bioactive Materials

Coating bioactive materials is another promising surface modification method for bioelectronics. Surface modification by coating bioactive materials such as hydrogels, bioactive molecules, and even cell layers contributes to reducing mechanical and electrical differences between the tissue and the electrode (**Figure 8*h***). Such coatings can improve long-term biocompatibility by releasing growth factors or chemical drugs, preventing biofoulings, or promoting cellular attachments. As a result, inflammatory reactions are reduced, and tissue regeneration is accelerated.

The coating of hydrogels on the electrode surface allows ionic flow, lowers impedance, and improves biocompatibility. For example, Ferlauto et al. (164) fabricated an electrode of PEDOT:PSS/platinum, on which a conductive alginate hydrogel was coated (**Figure 8*i***). Electrochemical and mechanical properties and EP performance of the 16-channel microelectrode array were analyzed. The conductive hydrogel coated on the PEDOT:PSS/Pt microelectrode showed enhanced mechanical (modulus of 12.29 ± 5.67 MPa) and electrochemical properties over the bare electrode. Specifically, the microelectrode had lower impedance (4.26 ± 0.29 kΩ at 1 kHz) and higher CSC (anodic: 12.96 ± 1.63 mC/cm^2, cathodic: 8.62 ± 0.90 mC/cm^2) than the bare Pt electrode or the PEDOT:PSS-coated Pt electrode. In vitro tests using human neural stem cells showed that the bioelectrode exhibited a lower noise level and better adhesion to tissues than the bare Pt electrode. To evaluate the electrode in vivo, it was implanted in the visual cortex of mice, and the visually evoked cortical potential was successfully recorded (**Figure 8*j***).

Abidian & Martin (165) developed a soft microelectrode with a modified surface, which can release biomaterials and maintain low impedance and high charge density. The microelectrode was coated with biodegradable nanofibers containing an anti-inflammatory drug (dexamethasone, DEX), and its surface was encapsulated with a layer of alginate hydrogel. Alginate hydrogel served as a mechanical buffer layer at the interface between the target neuron and the electrode. Then, electrochemical polymerization of the conducting polymer (PEDOT:PSS) was followed on the electrode surface (**Figure 8*k***). After these modifications, impedance decreased by ∼2 orders of magnitude (∼3 kΩ at 1 kHz), compared with the unmodified bare gold electrode (∼783 kΩ). The release profile of DEX was also studied (**Figure 8*l***). The coating of alginate hydrogel slowed the release rate of DEX, which prevented the burst release of DEX. This research presented a useful technique for fabricating a low-impedance electrode with controlled drug release capabilities.

Living cells have been applied to the surface coating of electrodes (166, 167), which mimics the mechanical properties and chemical compositions of target tissues (168) (**Figure 8*m***). For example, Green et al. (169) presented a soft cell–integrated electrode (known as a living electrode). Cell-loaded hydrogels were integrated with a Pt electrode. A nondegradable conductive hydrogel layer was deposited on the Pt electrode. Then, a cell-loaded (PC12 cell–loaded) degradable hydrogel layer was added on the conductive hydrogel layer. The layered hydrogels containing neurons supported excellent cell viability and differentiation in 12 days, while maintaining electrical conductivity. The living electrode showed advanced electrochemical properties, including low impedance (in the 100–1,000 Hz region), a high CSC of 50.00 ± 8.71 mC/cm^2 (control: 0.91 ± 0.16 mC/cm^2 for Pt and 24.96 ± 3.96 mC/cm^2 for conductive hydrogel), and a high cathodic charge injection limit of 0.83 ± 0.12 mC/cm^2 (control: 0.1 ± 0.05 mC/cm^2 for Pt) but low stiffness (modulus of ∼1 MPa).

In another example, Wise et al. (170) demonstrated a cell-encapsulated cochlear implant. Cell encapsulation of the electrode is supposed to prevent further degeneration of spiral ganglion neurons. The cochlear implant was coated with an alginate hydrogel containing choroid plexus cells (neurotrophins cells) and implanted in deafened neonatal cats. Each group of animals was treated by chronic electrical stimulation, neurotrophin cells, and their combinations for 8 months. The opposite ear served as a deafened control. The combined treatment with chronic electric stimulations and neurotrophin cells provided high spiral ganglion neuron survival in addition to increased peripheral process density (resprouting).

Serruya et al. (171) proposed a new concept of living electronics for neuromodulation, which constituted an implantable long-axonal living electrode and an external modulator. Excitatory (glutamatergic) neurons, dopaminergic neurons, and inhibitory (GABAergic) neurons filled a long hydrogel microcolumn (centimeter-scale length, hundreds of micrometers–scale diameter) to form an axonal living electrode (**Figure 8*n***). Only the living electrode was implanted

intracranially, whereas the optical/electrical modulation system was located in the extracranial region (**Figure 8*o***). Once implanted, the axon's spontaneous growth in the living electrode formed synaptic connections between the living electrode and the target neurons in the brain, which led to high biocompatibility in the long-term EP recording.

5. APPLICATIONS

The novel designs and materials introduced above have led to a plethora of wearable and implantable soft bioelectronics for the purposes of sensing and stimulation as well as delivering therapeutics. Various examples of wearable bioelectronics are introduced in the Supplemental Material (see **Supplemental Appendix 1**). In this section, we discuss wearable devices in terms of their sensing or stimulation modalities. For soft implantable bioelectronics, we introduce four representative applications: (*a*) EP sensing, (*b*) controlled drug delivery, (*c*) optical stimulation, and (*d*) electrical stimulation. Detailed explanations and examples are provided in **Supplemental Appendix 2**.

Supplemental Material >

6. SUMMARY AND FUTURE ASPECTS

The development of wearable and implantable soft bioelectronics has enabled high-quality biosignal recording and real-time feedback therapy. Key strategies for the development of such soft bioelectronics include novel device design, incorporation of soft materials, and surface treatment strategies. The deformable device design allows conformal integration of the device with the target tissue. The soft materials render the bioelectronics intrinsically deformable, which further improves intimate interfacing between the device and tissue. Surface treatments also improve the quality of device–tissue interfacing. Soft bioelectronics equipped with other therapeutic functions, such as controlled drug delivery, have also been introduced. These devices have maintained their designated performances reliably over a long-term period without biological side effects.

Although such research efforts have shown promise in soft wearable and implantable bioelectronics, challenges remain. First, fabrication techniques optimized for soft materials must be developed. Soft materials are often incompatible with conventional fabrication techniques, such as microelectromechanical systems (MEMS) processes. For example, many kinds of elastomers and hydrogels swell or degrade in the organic solvents and etchants that are typically used in MEMS processes. High-temperature processes, such as thermal evaporation for metal films, cause structural damage to soft materials. Plasma-based deposition of thin films causes damage to soft organic materials owing to ionic bombardment under plasma. Therefore, novel dry patterning methods, low-temperature deposition methods, and plasma-free fabrication processes compatible with soft materials should be developed.

Second, composite materials that consist of functional filler materials dispersed in the soft polymer matrix can face nonuniformity issues when patterned on extremely small scales. Current device technologies have achieved the design rule of electronics in the range of tens of nanometers. Random distribution of filler materials inside the soft polymeric media can meet the uniformity requirement when the device design rule is in the macroscale, such as at millimeter or micrometer scales. However, the irregular distribution of filler materials matters if the device design rule shrinks below the submicrometer scale. Thus, further development of nanoscale materials and optimization for their uniform dispersion in the polymer matrix are needed.

Third, medical-grade biocompatibility is needed for the commercialization of soft bioelectronic devices, especially for clinical translation of implantable devices. Novel soft materials must guarantee no notable cytotoxicity, which can be confirmed through further large-scale clinical

trials. Also, material degradation inside the human body can cause inflammatory reactions. In particular, degradation of encapsulation material can expose electronic components to ion-rich biofluids and enzymes, which accelerate material degradation and increase cytotoxicity. Therefore, the development of novel soft encapsulation materials with sufficiently low water and oxygen permeability, similar to levels found in conventional electronic-grade encapsulation materials, is required.

Fourth, further system optimization and device integration are needed. Currently, unit devices, such as sensors, stimulators, power supply modules, and data communication units, have been developed in soft, wearable, and implantable forms. However, they should be integrated into a system, and the system must be optimized for specific disease models to provide particular sensing and/or therapeutic functions. For such a goal, further miniaturization of the single device component and further development of advanced interconnection and packaging techniques are needed.

So far, novel soft materials and unconventional device design techniques have driven the development of soft bioelectronics and its applications to wearable and implantable biomedical devices. Such materials and devices will need to be upgraded and customized for specific applications and disease models in the future. Close collaborations between scientists in academia and industry, as well as clinicians, would accelerate such innovations. We hope that these research and development efforts bring breakthroughs in clinical protocols and healthcare industries.

DISCLOSURE STATEMENT

The authors are not aware of any affiliations, memberships, funding, or financial holdings that might be perceived as affecting the objectivity of this review. The views and conclusions contained in this document are those of the authors and should not be interpreted as representing the official policies, either expressed or implied, of the Army Research Office or the US Government.

ACKNOWLEDGMENTS

This work was supported by the Institute for Basic Science (IBS-R006-A1) of the Republic of Korea. N.L. acknowledges support from the US Office of Naval Research (ONR) under grant N00014-20-1-2112 and the US Army Research Office (ARO) under Cooperative Agreement W911NF-19-2-0333. The US Government is authorized to reproduce and distribute reprints for Government purposes notwithstanding any copyright notation herein. K.-H.H. acknowledges the Philip C. and Linda L. Lewis Foundation Graduate Fellowship at the University of Texas at Austin.

LITERATURE CITED

1. Reportlinker. 2018. Wearable medical devices global market opportunities and strategies to 2022. *Newswire PR*, Aug. 15. **https://www.prnewswire.com/news-releases/wearable-medical-devices-global-market-opportunities-and-strategies-to-2022-300697842.html**
2. Shi H, Zhao H, Liu Y, Gao W, Dou S-C. 2019. Systematic analysis of a military wearable device based on a multi-level fusion framework: research directions. *Sensors* 19(12):2651
3. Koo JH, Song J, Yoo S, Sunwoo S, Son D, Kim D. 2020. Unconventional device and material approaches for monolithic biointegration of implantable sensors and wearable electronics. *Adv. Mater. Technol.* 5(10):e2000407
4. Yin Y, Zeng Y, Chen X, Fan Y. 2016. The internet of things in healthcare: an overview. *J. Ind. Inf. Integr.* 1:3–13
5. Choi C, Choi MK, Hyeon T, Kim D-H. 2016. Nanomaterial-based soft electronics for healthcare applications. *ChemNanoMat* 2(11):1006–17

6. Anzaldo D. 2015. Wearable sports technology—market landscape and compute SoC trends. In *Proceedings of the 2015 International SoC Design Conference*. Piscataway, NJ: IEEE
7. Lim S, Son D, Kim J, Lee YB, Song J-K, et al. 2015. Transparent and stretchable interactive human machine interface based on patterned graphene heterostructures. *Adv. Funct. Mater.* 25(3):375–83
8. Pang Y, Yang Z, Yang Y, Ren T. 2020. Wearable electronics based on 2D materials for human physiological information detection. *Small* 16(15):1901124
9. Gao Y, Yu L, Yeo JC, Lim CT. 2020. Flexible hybrid sensors for health monitoring: materials and mechanisms to render wearability. *Adv. Mater.* 32(15):1902133
10. Amjadi M, Sheykhansari S, Nelson BJ, Sitti M. 2018. Recent advances in wearable transdermal delivery systems. *Adv. Mater.* 30(7):1704530
11. Kaewkannate K, Kim S. 2016. A comparison of wearable fitness devices. *BMC Public Health* 16:433
12. Kutilek P, Volf P, Viteckova S, Smrcka P, Krivanek V, et al. 2017. Wearable systems for monitoring the health condition of soldiers: review and application. In *Proceedings of the 2017 International Conference on Military Technologies.* Piscataway, NJ: IEEE
13. O'Neill CT, Phipps NS, Cappello L, Paganoni S, Walsh CJ. 2017. A soft wearable robot for the shoulder: Design, characterization, and preliminary testing. In *Proceedings of the 2017 International Conference on Rehabilitation Robotics*. Piscataway, NJ: IEEE
14. In H, Kang BB, Sin M, Cho K-J. 2015. Exo-Glove: a wearable robot for the hand with a soft tendon routing system. *IEEE Robot. Autom. Mag.* 22(1):97–105
15. Chambers R, Gabbett TJ, Cole MH, Beard A. 2015. The use of wearable microsensors to quantify sport-specific movements. *Sport. Med.* 45(7):1065–81
16. Hegde N, Bries M, Sazonov E. 2016. A comparative review of footwear-based wearable systems. *Electronics* 5(3):48
17. Wood J. 2017. Revolutions in wearable technology for apparel. In *High-Performance Apparel*, ed. J McLoughlin, T Sabir, pp. 325–39. Cambridge, MA: Woodhead Publ.
18. Awolusi I, Marks E, Hallowell M. 2018. Wearable technology for personalized construction safety monitoring and trending: review of applicable devices. *Autom. Constr.* 85:96–106
19. Kritzler M, Bäckman M, Tenfält A, Michahelles F. 2015. Wearable technology as a solution for workplace safety. In *MUM '15: Proceedings of the 14th International Conference on Mobile and Ubiquitous Multimedia*, pp. 213–17. New York: Assoc. Comput. Mach.
20. Song Y, Min J, Gao W. 2019. Wearable and implantable electronics: moving toward precision therapy. *ACS Nano* 13(11):12280–86
21. Koydemir HC, Ozcan A. 2018. Wearable and implantable sensors for biomedical applications. *Annu. Rev. Anal. Chem.* 11:127–46
22. Corduas F, Mancuso E, Lamprou DA. 2020. Long-acting implantable devices for the prevention and personalised treatment of infectious, inflammatory and chronic diseases. *J. Drug Deliv. Sci. Technol.* 60:101952
23. Sunwoo SH, Lee JS, Bae S, Shin YJ, Kim CS, et al. 2019. Chronic and acute stress monitoring by electrophysiological signals from adrenal gland. *PNAS* 116(4):1146–51
24. Ouyang H, Liu Z, Li N, Shi B, Zou Y, et al. 2019. Symbiotic cardiac pacemaker. *Nat. Commun.* 10:1821
25. Gutruf P, Yin RT, Lee KB, Ausra J, Brennan JA, et al. 2019. Wireless, battery-free, fully implantable multimodal and multisite pacemakers for applications in small animal models. *Nat. Commun.* 10:5742
26. Son D, Lee J, Lee DJ, Ghaffari R, Yun S, et al. 2015. Bioresorbable electronic stent integrated with therapeutic nanoparticles for endovascular diseases. *ACS Nano* 9(6):5937–46
27. Li C, Guo C, Fitzpatrick V, Ibrahim A, Zwierstra MJ, et al. 2020. Design of biodegradable, implantable devices towards clinical translation. *Nat. Rev. Mater.* 5:61–81
28. Brouwer TF, Yilmaz D, Lindeboom R, Buiten MS, Olde Nordkamp LRA, et al. 2016. Long-term clinical outcomes of subcutaneous versus transvenous implantable defibrillator therapy. *J. Am. Coll. Cardiol.* 68(19):2047–55
29. Deshmukh A, Brown L, Barbe MF, Braverman AS, Tiwari E, et al. 2020. Fully implantable neural recording and stimulation interfaces: peripheral nerve interface applications. *J. Neurosci. Methods* 333:108562
30. Lee JH, Kim H, Kim JH, Lee S-HH. 2016. Soft implantable microelectrodes for future medicine: prosthetics, neural signal recording and neuromodulation. *Lab Chip* 16(6):959–76

31. Sunwoo SH, Kim T. 2016. Materials and designs for multimodal flexible neural probes. In *Stretchable Bioelectronics for Medical Devices and Systems*, ed. J Rogers, R Ghaffari, DH Kim, pp. 293–308. Cham, Switz.: Springer
32. Kim MS, Lee GJ, Choi C, Kim MS, Lee M, et al. 2020. An aquatic-vision-inspired camera based on a monocentric lens and a silicon nanorod photodiode array. *Nat. Electron.* 3(9):546–53
33. Choi G, Song Y, Lim H, Lee SH, Lee HK, et al. 2020. Antibacterial nanopillar array for an implantable intraocular lens. *Adv. Healthc. Mater.* 9(18):2000447
34. Gesing AL, Alves FDP, Paul S, Cordioli JA. 2018. On the design of a MEMS piezoelectric accelerometer coupled to the middle ear as an implantable sensor for hearing devices. *Sci. Rep.* 8:3920
35. Pons-Faudoa FP, Ballerini A, Sakamoto J, Grattoni A. 2019. Advanced implantable drug delivery technologies: transforming the clinical landscape of therapeutics for chronic diseases. *Biomed. Microdevices* 21(2):47
36. Cha GD, Kang D, Lee J, Kim DH. 2019. Bioresorbable electronic implants: history, materials, fabrication, devices, and clinical applications. *Adv. Healthc. Mater.* 8(11):1801660
37. Sardu C, Marfella R, Santamaria M, Papini S, Parisi Q, et al. 2018. Stretch, injury and inflammation markers evaluation to predict clinical outcomes after implantable cardioverter defibrillator therapy in heart failure patients with metabolic syndrome. *Front. Physiol.* 9:758
38. Smith D. 2003. Postoperative inflammation after implantation of the implantable contact lens. *Ophthalmology* 110(12):2335–41
39. Ling Y, An T, Yap LW, Zhu B, Gong S, Cheng W. 2020. Disruptive, soft, wearable sensors. *Adv. Mater.* 32(18):1904664
40. Drees C, Makic MB, Case K, Mancuso MP, Hill A, et al. 2016. Skin irritation during video-EEG monitoring. *Neurodiagn. J.* 56(3):139–50
41. Lau-Zhu A, Lau MPH, McLoughlin G. 2019. Mobile EEG in research on neurodevelopmental disorders: opportunities and challenges. *Dev. Cogn. Neurosci.* 36:100635
42. Lee SM, Kim JH, Park C, Hwang J-YY, Hong JS, et al. 2016. Self-adhesive and capacitive carbon nanotube-based electrode to record electroencephalograph signals from the hairy scalp. *IEEE Trans. Biomed. Eng.* 63(1):138–47
43. Zou Y, Dehzangi O, Nathan V, Jafari R. 2014. Automatic removal of EEG artifacts using electrode-scalp impedance. In *Proceedings of the 2014 IEEE International Conference on Acoustics, Speech and Signal Processing*. Piscataway, NJ: IEEE
44. Someya T, Bao Z, Malliaras GG. 2016. The rise of plastic bioelectronics. *Nature* 540(7633):379–85
45. Feron K, Lim R, Sherwood C, Keynes A, Brichta A, Dastoor PC. 2018. Organic bioelectronics: materials and biocompatibility. *Int. J. Mol. Sci.* 19(8):2382
46. Pan L, Wang F, Cheng Y, Leow WR, Zhang YW, et al. 2020. A supertough electro-tendon based on spider silk composites. *Nat. Commun.* 11:1332
47. Prodanov D, Delbeke J. 2016. Mechanical and biological interactions of implants with the brain and their impact on implant design. *Front. Neurosci.* 10:11
48. Bhattarai SR, Bhattarai N, Viswanathamurthi P, Yi HK, Hwang PH, Kim HY. 2006. Hydrophilic nanofibrous structure of polylactide; fabrication and cell affinity. *J. Biomed. Mater. Res. A* 78(2):247–57
49. Nolta NF, Ghelich P, Han M. 2019. Recessed traces for planarized passivation of chronic neural microelectrodes. *Conf. Proc. IEEE Eng. Med. Biol. Soc.* 2019:5125–28
50. Abidian MR, Martin DC. 2008. Experimental and theoretical characterization of implantable neural microelectrodes modified with conducting polymer nanotubes. *Biomaterials* 29(9):1273–83
51. Lee Y, Kim J, Koo JH, Kim TH, Kim DH. 2018. Nanomaterials for bioelectronics and integrated medical systems. *Korean J. Chem. Eng.* 35:1–11
52. Lee Y, Kim J, Joo H, Raj MS, Ghaffari R, Kim D-H. 2017. Wearable sensing systems with mechanically soft assemblies of nanoscale materials. *Adv. Mater. Technol.* 2(9):1700053
53. Hong S, Lee S, Kim D-H. 2019. Materials and design strategies of stretchable electrodes for electronic skin and its applications. *Proc. IEEE* 107(10):2185–97
54. Rogers JA, Someya T, Huang Y. 2010. Materials and mechanics for stretchable electronics. *Science* 327(5973):1603–7

55. Lu N, Yang S. 2015. Mechanics for stretchable sensors. *Curr. Opin. Solid State Mater. Sci.* 19(3):149–59
56. Nassar JM, Rojas JP, Hussain AM, Hussain MM. 2016. From stretchable to reconfigurable inorganic electronics. *Extreme Mech. Lett.* 9:245–68
57. Wang C, Wang C, Huang Z, Xu S. 2018. Materials and structures toward soft electronics. *Adv. Mater.* 30(50):1801368
58. Jang H, Dai Z, Ha K-H, Ameri SK, Lu N. 2019. Stretchability of PMMA-supported CVD graphene and of its electrical contacts. *2D Mater.* 7:014003
59. Arab Hassani F, Jin H, Yokota T, Someya T, Thakor NV. 2020. Soft sensors for a sensing-actuation system with high bladder voiding efficiency. *Sci. Adv.* 6(18):eaba0412
60. Qi D, Liu Z, Yu M, Liu Y, Tang Y, et al. 2015. Highly stretchable gold nanobelts with sinusoidal structures for recording electrocorticograms. *Adv. Mater.* 27(20):3145–51
61. Li T, Suo Z, Lacour SP, Wagner S. 2005. Compliant thin film patterns of stiff materials as platforms for stretchable electronics. *J. Mater. Res.* 20(12):3274–77
62. Gray DS, Tien J, Chen CS. 2004. High-conductivity elastomeric electronics. *Adv. Mater.* 16(5):393–97
63. Hsu Y-Y, Gonzalez M, Bossuyt F, Axisa F, Vanfleteren J, De Wolf I. 2009. In situ observations on deformation behavior and stretching-induced failure of fine pitch stretchable interconnect. *J. Mater. Res.* 24(12):3573–82
64. Hsu Y-Y, Gonzalez M, Bossuyt F, Vanfleteren J, De Wolf I. 2011. Polyimide-enhanced stretchable interconnects: design, fabrication, and characterization. *IEEE Trans. Electron Devices* 58(8):2680–88
65. Su Y, Wu J, Fan Z, Hwang K-C, Song J, et al. 2012. Postbuckling analysis and its application to stretchable electronics. *J. Mech. Phys. Solids* 60(3):487–508
66. Zhang Y, Xu S, Fu H, Lee J, Su J, et al. 2013. Buckling in serpentine microstructures and applications in elastomer-supported ultra-stretchable electronics with high areal coverage. *Soft Matter* 9(33):8062–70
67. Widlund T, Yang S, Hsu Y-Y, Lu N. 2014. Stretchability and compliance of freestanding serpentine-shaped ribbons. *Int. J. Solids Struct.* 51(23–24):4026–37
68. Xu S, Zhang Y, Jia L, Mathewson KE, Jang K-I, et al. 2014. Soft microfluidic assemblies of sensors, circuits, and radios for the skin. *Science* 344(6179):70–74
69. Yang S, Chen Y-C, Nicolini L, Pasupathy P, Sacks J, et al. 2015. "Cut-and-paste" manufacture of multiparametric epidermal sensor systems. *Adv. Mater.* 27(41):6423–30
70. Jeong H, Wang L, Ha T, Mitbander R, Yang X, et al. 2019. Modular and reconfigurable wireless e-tattoos for personalized sensing. *Adv. Mater. Technol.* 4(8):1900117
71. Fan JA, Yeo W-H, Su Y, Hattori Y, Lee W, et al. 2014. Fractal design concepts for stretchable electronics. *Nat. Commun.* 5:3266
72. Xu S, Zhang Y, Cho J, Lee J, Huang X, et al. 2013. Stretchable batteries with self-similar serpentine interconnects and integrated wireless recharging systems. *Nat. Commun.* 4:1543
73. Jeong J-W, Kim MK, Cheng H, Yeo W-H, Huang X, et al. 2014. Capacitive epidermal electronics for electrically safe, long-term electrophysiological measurements. *Adv. Healthc. Mater.* 3(5):642–48
74. Jang K-I, Chung HU, Xu S, Lee CH, Luan H, et al. 2015. Soft network composite materials with deterministic and bio-inspired designs. *Nat. Commun.* 6:6566
75. Liu Z, Yu M, Lv J, Li Y, Yu Z. 2014. Dispersed, porous nanoislands landing on stretchable nanocrack gold films: maintenance of stretchability and controllable impedance. *ACS Appl. Mater. Interfaces* 6(16):13487–95
76. Vachicouras N, Tringides CM, Campiche PB, Lacour SP. 2017. Engineering reversible elasticity in ductile and brittle thin films supported by a plastic foil. *Extreme Mech. Lett.* 15:63–69
77. Vachicouras N, Tarabichi O, Kanumuri VV, Tringides CM, Macron J, et al. 2019. Microstructured thin-film electrode technology enables proof of concept of scalable, soft auditory brainstem implants. *Sci. Transl. Med.* 11(514):eaax9487
78. Jang N-S, Kim K-H, Ha S-H, Jung S-H, Lee HM, Kim J-M. 2017. Simple approach to high-performance stretchable heaters based on kirigami patterning of conductive paper for wearable thermotherapy applications. *ACS Appl. Mater. Interfaces* 9(23):19612–21
79. Wang L, Qiao S, Ameri SK, Jeong H, Lu N. 2017. A thin elastic membrane conformed to a soft and rough substrate subjected to stretching/compression. *J. Appl. Mech.* 84(11):111003

80. Wang L, Lu N. 2016. Conformability of a thin elastic membrane laminated on a soft substrate with slightly wavy surface. *J. Appl. Mech.* 83(4):041007
81. Cheng H, Wang S. 2014. Mechanics of interfacial delamination in epidermal electronics systems. *J. Appl. Mech.* 81(4):044501
82. Wang S, Li M, Wu J, Kim D-H, Lu N, et al. 2012. Mechanics of epidermal electronics. *J. Appl. Mech.* 79(3):031022
83. Kim J, Son D, Lee M, Song C, Song J-K, et al. 2016. A wearable multiplexed silicon nonvolatile memory array using nanocrystal charge confinement. *Sci. Adv.* 2(1):e1501101
84. Son D, Chae SI, Kim M, Choi MK, Yang J, et al. 2016. Colloidal synthesis of uniform-sized molybdenum disulfide nanosheets for wafer-scale flexible nonvolatile memory. *Adv. Mater.* 28(42):9326–32
85. Kim J, Shim HJ, Yang J, Choi MK, Kim DC, et al. 2017. Ultrathin quantum dot display integrated with wearable electronics. *Adv. Mater.* 29(38):1700217
86. Jeong J-W, Yeo W-H, Akhtar A, Norton JJS, Kwack Y-J, et al. 2013. Materials and optimized designs for human-machine interfaces via epidermal electronics. *Adv. Mater.* 25(47):6839–46
87. Ameri SK, Kim M, Kuang IA, Perera WK, Alshiekh M, et al. 2018. Imperceptible electrooculography graphene sensor system for human-robot interface. *npj 2D Mater. Appl.* 2:19
88. Kim D-H, Viventi J, Amsden JJ, Xiao J, Vigeland L, et al. 2010. Dissolvable films of silk fibroin for ultrathin conformal bio-integrated electronics. *Nat. Mater.* 9(6):511–17
89. Autumn K, Liang YA, Hsieh ST, Zesch W, Chan WP, et al. 2000. Adhesive force of a single gecko foot-hair. *Nature* 405(6787):681–85
90. Sahay R, Low HY, Baji A, Foong S, Wood KL. 2015. A state-of-the-art review and analysis on the design of dry adhesion materials for applications such as climbing micro-robots. *RSC Adv.* 5(63):50821–32
91. Boesel LF, Greiner C, Arzt E, del Campo A. 2010. Gecko-inspired surfaces: a path to strong and reversible dry adhesives. *Adv. Mater.* 22(19):2125–37
92. Kamperman M, Kroner E, del Campo A, McMeeking RM, Arzt E. 2010. Functional adhesive surfaces with "gecko" effect: the concept of contact splitting. *Adv. Eng. Mater.* 12(5):335–48
93. Yao H, Gao H. 2006. Mechanics of robust and releasable adhesion in biology: bottom-up designed hierarchical structures of gecko. *J. Mech. Phys. Solids* 54(6):1120–46
94. Pang C, Koo JH, Nguyen A, Caves JM, Kim M-G, et al. 2015. Highly skin-conformal microhairy sensor for pulse signal amplification. *Adv. Mater.* 27(4):634–40
95. Kim T, Park J, Sohn J, Cho D, Jeon S. 2016. Bioinspired, highly stretchable, and conductive dry adhesives based on 1D-2D hybrid carbon nanocomposites for all-in-one ECG electrodes. *ACS Nano* 10(4):4770–78
96. Choi MK, Park OK, Choi C, Qiao S, Ghaffari R, et al. 2016. Cephalopod-inspired miniaturized suction cups for smart medical skin. *Adv. Healthc. Mater.* 5(1):80–87
97. Ying M, Bonifas AP, Lu N, Su Y, Li R, et al. 2012. Silicon nanomembranes for fingertip electronics. *Nanotechnology* 23(34):344004
98. Xu L, Gutbrod SR, Bonifas AP, Su Y, Sulkin MS, et al. 2014. 3D multifunctional integumentary membranes for spatiotemporal cardiac measurements and stimulation across the entire epicardium. *Nat. Commun.* 5:3329
99. Park J, Choi S, Janardhan AH, Lee S-YY, Raut S, et al. 2016. Electromechanical cardioplasty using a wrapped elasto-conductive epicardial mesh. *Sci. Transl. Med.* 8(344):344ra86
100. Choi C, Choi MK, Liu S, Kim MS, Park OK, et al. 2017. Human eye-inspired soft optoelectronic device using high-density MoS_2-graphene curved image sensor array. *Nat. Commun.* 8:1664
101. Kim D-H, Lu N, Ghaffari R, Kim Y-S, Lee SP, et al. 2011. Materials for multifunctional balloon catheters with capabilities in cardiac electrophysiological mapping and ablation therapy. *Nat. Mater.* 10(4):316–23
102. Zhang Y, Zheng N, Cao Y, Wang F, Wang P, et al. 2019. Climbing-inspired twining electrodes using shape memory for peripheral nerve stimulation and recording. *Sci. Adv.* 5(4):eaaw1066
103. Liu J, Fu TM, Cheng Z, Hong G, Zhou T, et al. 2015. Syringe-injectable electronics. *Nat. Nanotechnol.* 10(7):629–35
104. Zhou T, Hong G, Fu T-M, Yang X, Schuhmann TG, et al. 2017. Syringe-injectable mesh electronics integrate seamlessly with minimal chronic immune response in the brain. *PNAS* 114(23):5894–99

105. Fu T-M, Hong G, Zhou T, Schuhmann TG, Viveros RD, Lieber CM. 2016. Stable long-term chronic brain mapping at the single-neuron level. *Nat. Methods* 13(10):875–82
106. Tian B, Liu J, Dvir T, Jin L, Tsui JH, et al. 2012. Macroporous nanowire nanoelectronic scaffolds for synthetic tissues. *Nat. Mater.* 11:986–94
107. Xie C, Liu J, Fu TM, Dai X, Zhou W, Lieber CM. 2015. Three-dimensional macroporous nanoelectronic networks as minimally invasive brain probes. *Nat. Mater.* 14(12):1286–92
108. Wang X, Guo X, Ye J, Zheng N, Kohli P, et al. 2019. Freestanding 3D mesostructures, functional devices, and shape-programmable systems based on mechanically induced assembly with shape memory polymers. *Adv. Mater.* 31(2):1805615
109. Xu S, Yan Z, Jang K-I, Huang W, Fu H, et al. 2015. Assembly of micro/nanomaterials into complex, three-dimensional architectures by compressive buckling. *Science* 347(6218):154–59
110. Wang X, Feiner R, Luan H, Zhang Q, Zhao S, et al. 2020. Three-dimensional electronic scaffolds for monitoring and regulation of multifunctional hybrid tissues. *Extrem. Mech. Lett.* 35:100634
111. Yan Z, Han M, Shi Y, Badea A, Yang Y, et al. 2017. Three-dimensional mesostructures as high-temperature growth templates, electronic cellular scaffolds, and self-propelled microrobots. *PNAS* 114(45):E9455–64
112. Li Q, Nan K, Le Floch P, Lin Z, Sheng H, et al. 2019. Cyborg organoids: implantation of nanoelectronics via organogenesis for tissue-wide electrophysiology. *Nano Lett.* 19(8):5781–89
113. Kim DC, Shim HJ, Lee W, Koo JH, Kim D-H. 2020. Material-based approaches for the fabrication of stretchable electronics. *Adv. Mater.* 32(15):1902743
114. Guo R, Liu J. 2017. Implantable liquid metal-based flexible neural microelectrode array and its application in recovering animal locomotion functions. *J. Micromech. Microeng.* 27(10):104002
115. Ota H, Chen K, Lin Y, Kiriya D, Shiraki H, et al. 2014. Highly deformable liquid-state heterojunction sensors. *Nat. Commun.* 5:5032
116. Wen X, Wang B, Huang S, Liu TL, Lee M-S, et al. 2019. Flexible, multifunctional neural probe with liquid metal enabled, ultra-large tunable stiffness for deep-brain chemical sensing and agent delivery. *Biosens. Bioelectron.* 131:37–45
117. Gannarapu A, Gozen BA. 2016. Freeze-printing of liquid metal alloys for manufacturing of 3D, conductive, and flexible networks. *Adv. Mater. Technol.* 1(4):1600047
118. Choi MK, Park I, Kim DC, Joh E, Park OK, et al. 2015. Thermally controlled, patterned graphene transfer printing for transparent and wearable electronic/optoelectronic system. *Adv. Funct. Mater.* 25(46):7109–18
119. Son D, Koo JH, Song JK, Kim J, Lee M, et al. 2015. Stretchable carbon nanotube charge-trap floating-gate memory and logic devices for wearable electronics. *ACS Nano* 9(5):5585–93
120. Kim J, Ghaffari R, Kim D-H. 2017. The quest for miniaturized soft bioelectronic devices. *Nat. Biomed. Eng.* 1:0049
121. Koo JH, Song J-K, Kim D-H. 2019. Solution-processed thin films of semiconducting carbon nanotubes and their application to soft electronics. *Nanotechnology* 30(13):132001
122. Lee E, Kim HJ, Park Y, Lee S, Lee SY, et al. 2019. Direct patterning of a carbon nanotube thin layer on a stretchable substrate. *Micromachines* 10(8):530
123. Gilshteyn EP, Lin S, Kondrashov VA, Kopylova DS, Tsapenko AP, et al. 2018. A one-step method of hydrogel modification by single-walled carbon nanotubes for highly stretchable and transparent electronics. *ACS Appl. Mater. Interfaces* 10(33):28069–75
124. Li X, Li Y, Guan T, Xu F, Sun J. 2018. Durable, highly electrically conductive cotton fabrics with healable superamphiphobicity. *ACS Appl. Mater. Interfaces* 10(14):12042–50
125. Yang M, Pan J, Xu A, Luo L, Cheng D, et al. 2018. Conductive cotton fabrics for motion sensing and heating applications. *Polymers* 10(6):568
126. Lin Z-I, Lou C-W, Pan Y-J, Hsieh C-T, Huang C-H, et al. 2017. Conductive fabrics made of polypropylene/multi-walled carbon nanotube coated polyester yarns: mechanical properties and electromagnetic interference shielding effectiveness. *Compos. Sci. Technol.* 141:74–82
127. Hu L, Pasta M, La Mantia F, Cui L, Jeong S, et al. 2010. Stretchable, porous, and conductive energy textiles. *Nano Lett.* 10(2):708–14

128. Jia L-C, Xu L, Ren F, Ren P-G, Yan D-X, Li Z-M. 2019. Stretchable and durable conductive fabric for ultrahigh performance electromagnetic interference shielding. *Carbon* 144:101–8
129. Tseghai GB, Mengistie DA, Malengier B, Fante KA, Van Langenhove L. 2020. PEDOT:PSS-based conductive textiles and their applications. *Sensors* 20(7):1881
130. Tadesse MG, Mengistie DA, Chen Y, Wang L, Loghin C, Nierstrasz V. 2019. Electrically conductive highly elastic polyamide/lycra fabric treated with PEDOT:PSS and polyurethane. *J. Mater. Sci.* 54:9591–602
131. Song W-L, Gong C, Li H, Cheng X-D, Chen M, et al. 2017. Graphene-based sandwich structures for frequency selectable electromagnetic shielding. *ACS Appl. Mater. Interfaces* 9(41):36119–29
132. Zhao Z, Huang Q, Yan C, Liu Y, Zeng X, et al. 2020. Machine-washable and breathable pressure sensors based on triboelectric nanogenerators enabled by textile technologies. *Nano Energy* 70:104528
133. Ganji M, Tanaka A, Gilja V, Halgren E, Dayeh SA. 2017. Scaling effects on the electrochemical stimulation performance of Au, Pt, and PEDOT:PSS electrocorticography arrays. *Adv. Funct. Mater.* 27(42):1703019
134. Ganji M, Elthakeb AT, Tanaka A, Gilja V, Halgren E, Dayeh SA. 2017. Scaling effects on the electrochemical performance of poly(3,4-ethylenedioxythiophene (PEDOT), Au, and Pt for electrocorticography recording. *Adv. Funct. Mater.* 27(42):1703018
135. Ganji M, Kaestner E, Hermiz J, Rogers N, Tanaka A, et al. 2018. Development and translation of PEDOT:PSS microelectrodes for intraoperative monitoring. *Adv. Funct. Mater.* 28(12):1700232
136. Wang Y, Zhu C, Pfattner R, Yan H, Jin L, et al. 2017. A highly stretchable, transparent, and conductive polymer. *Sci. Adv.* 3(3):e1602076
137. Fang Y, Li Y, Li Y, Ding M, Xie J, Hu B. 2020. Solution-processed submicron free-standing, conformal, transparent, breathable epidermal electrodes. *ACS Appl. Mater. Interfaces* 12(21):23689–96
138. Lu B, Yuk H, Lin S, Jian N, Qu K, et al. 2019. Pure PEDOT:PSS hydrogels. *Nat. Commun.* 10:1043
139. Aregueta-Robles UA, Woolley AJ, Poole-Warren LA, Lovell NH, Green RA. 2014. Organic electrode coatings for next-generation neural interfaces. *Front. Neuroeng.* 7:15
140. Cha GD, Lee WH, Lim C, Choi MK, Kim D-HH. 2020. Materials engineering, processing, and device application of hydrogel nanocomposites. *Nanoscale* 12(19):10456–73
141. Choi S, Han SI, Kim D, Hyeon T, Kim D-H. 2019. High-performance stretchable conductive nanocomposites: materials, processes, and device applications. *Chem. Soc. Rev.* 48(6):1566–95
142. Wang H, Biswas SK, Zhu S, Lu Y, Yue Y, et al. 2020. Self-healable electro-conductive hydrogels based on core-shell structured nanocellulose/carbon nanotubes hybrids for use as flexible supercapacitors. *Nanomaterials* 10(1):112
143. Liu Y, Liu J, Chen S, Lei T, Kim Y, et al. 2019. Soft and elastic hydrogel-based microelectronics for localized low-voltage neuromodulation. *Nat. Biomed. Eng.* 3:58–68
144. Choi C, Lee Y, Cho KW, Koo JH, Kim D-H. 2019. Wearable and implantable soft bioelectronics using two-dimensional materials. *Acc. Chem. Res.* 52(1):73–81
145. Nam J, Lim HK, Kim NH, Park JK, Kang ES, et al. 2020. Supramolecular peptide hydrogel-based soft neural interface augments brain signals through a three-dimensional electrical network. *ACS Nano* 14(1):664–75
146. Lim C, Shin Y, Jung J, Kim JH, Lee S, Kim DH. 2019. Stretchable conductive nanocomposite based on alginate hydrogel and silver nanowires for wearable electronics. *APL Mater.* 7(3):031502
147. Hong S, Lee J, Do K, Lee M, Kim JH, et al. 2017. Stretchable electrode based on laterally combed carbon nanotubes for wearable energy harvesting and storage devices. *Adv. Funct. Mater.* 27(48):1704353
148. Joo H, Jung D, Sunwoo S-H, Koo JH, Kim D-H. 2020. Material design and fabrication strategies for stretchable metallic nanocomposites. *Small* 16(11):1906270
149. Du J, Wang L, Shi Y, Zhang F, Hu S, et al. 2020. Optimized CNT-PDMS flexible composite for attachable health-care device. *Sensors* 20(16):4523
150. Lind JU, Busbee TA, Valentine AD, Pasqualini FS, Yuan H, et al. 2017. Instrumented cardiac microphysiological devices via multimaterial three-dimensional printing. *Nat. Mater.* 16(3):303–8
151. Chu M, Nguyen T, Pandey V, Zhou Y, Pham HN, et al. 2019. Respiration rate and volume measurements using wearable strain sensors. *npj Digit. Med.* 2:8

152. Ren M, Zhou Y, Wang Y, Zheng G, Dai K, et al. 2019. Highly stretchable and durable strain sensor based on carbon nanotubes decorated thermoplastic polyurethane fibrous network with aligned wave-like structure. *Chem. Eng. J.* 360:762–77
153. Zhou X, Zhu L, Fan L, Deng H, Fu Q. 2018. Fabrication of highly stretchable, washable, wearable, water-repellent strain sensors with multi-stimuli sensing ability. *ACS Appl. Mater. Interfaces* 10(37):31655–63
154. Song Y, Chen H, Chen X, Wu H, Guo H, et al. 2018. All-in-one piezoresistive-sensing patch integrated with micro-supercapacitor. *Nano Energy* 53:189–97
155. Zheng Y, Li Y, Dai K, Wang Y, Zheng G, et al. 2018. A highly stretchable and stable strain sensor based on hybrid carbon nanofillers/polydimethylsiloxane conductive composites for large human motions monitoring. *Compos. Sci. Technol.* 156:276–86
156. Dang Z-M, Yuan J-K, Zha J-W, Zhou T, Li S-T, Hu G-H. 2012. Fundamentals, processes and applications of high-permittivity polymer-matrix composites. *Prog. Mater. Sci.* 57(4):660–723
157. Matsuhisa N, Inoue D, Zalar P, Jin H, Matsuba Y, et al. 2017. Printable elastic conductors by *in situ* formation of silver nanoparticles from silver flakes. *Nat. Mater.* 16(8):834–40
158. Choi S, Han SI, Jung D, Hwang HJ, Lim C, et al. 2018. Highly conductive, stretchable and biocompatible Ag-Au core-sheath nanowire composite for wearable and implantable bioelectronics. *Nat. Nanotechnol.* 13(11):1048–56
159. Sunwoo SH, Han SI, Kang H, Cho YS, Jung D, et al. 2020. Stretchable low-impedance nanocomposite comprised of Ag-Au core-shell nanowires and Pt black for epicardial recording and stimulation. *Adv. Mater. Technol.* 5(3):1900768
160. Liu Z, Wang H, Huang P, Huang J, Zhang Y, et al. 2019. Highly stable and stretchable conductive films through thermal-radiation-assisted metal encapsulation. *Adv. Mater.* 31(35):1901360
161. Ereifej ES, Smith CS, Meade SM, Chen K, Feng H, Capadona JR. 2018. The neuroinflammatory response to nanopatterning parallel grooves into the surface structure of intracortical microelectrodes. *Adv. Funct. Mater.* 28(12):1704420
162. Buzsaki G. 2004. Neuronal oscillations in cortical networks. *Science* 304(5679):1926–29
163. Kim E, Kim J-Y, Choi H. 2017. An SU-8-based microprobe with a nanostructured surface enhances neuronal cell attachment and growth. *Micro Nano Syst. Lett.* 5:28
164. Ferlauto L, D'Angelo AN, Vagni P, Airaghi Leccardi MJI, Mor FM, et al. 2018. Development and characterization of PEDOT:PSS/alginate soft microelectrodes for application in neuroprosthetics. *Front. Neurosci.* 12:648
165. Abidian MR, Martin DC. 2009. Multifunctional nanobiomaterials for neural interfaces. *Adv. Funct. Mater.* 19(4):573–85
166. Kim SJ, Cho HR, Cho KW, Qiao S, Rhim JS, et al. 2015. Multifunctional cell-culture platform for aligned cell sheet monitoring, transfer printing, and therapy. *ACS Nano* 9(3):2677–88
167. Cho KW, Kim SJ, Kim J, Song SY, Lee WH, et al. 2019. Large scale and integrated platform for digital mass culture of anchorage dependent cells. *Nat. Commun.* 10:4824
168. Kim SJ, Cho KW, Cho HR, Wang L, Park SY, et al. 2016. Stretchable and transparent biointerface using cell-sheet-graphene hybrid for electrophysiology and therapy of skeletal muscle. *Adv. Funct. Mater.* 26(19):3207–17
169. Green RA, Lim KS, Henderson WC, Hassarati RT, Martens PJ, et al. 2013. Living electrodes: tissue engineering the neural interface. In *Proceedings of the 35th Annual International Conference of the IEEE Engineering in Medicine and Biology Society (EMBC)*, pp. 6957–60. Piscataway, NJ: IEEE
170. Wise AK, Fallon JB, Neil AJ, Pettingill LN, Geaney MS, et al. 2011. Combining cell-based therapies and neural prostheses to promote neural survival. *Neurotherapeutics* 8(4):774–87
171. Serruya MD, Harris JP, Adewole DO, Struzyna LA, Burrell JC, et al. 2018. Engineered axonal tracts as "living electrodes" for synaptic-based modulation of neural circuitry. *Adv. Funct. Mater.* 28(12):e1701183

Annual Review of Chemical and Biomolecular Engineering

Volume 12, 2021

Contents

Errata

An online log of corrections to *Annual Review of Chemical and Biomolecular Engineering* articles may be found at http://www.annualreviews.org/errata/chembioeng

Supplemental Material: Annu. Rev. Chem. Biomol. Eng. 2021. 12.
https://doi.org/10.1146/annurev-chembioeng-101420-024336
Wearable and Implantable Soft Bioelectronics: Device Designs and Material Strategies
Sunwoo, Ha, Lee, Lu, and Kim

Supplemental Appendix 1

Wearable Bioelectronics

1. Electrical sensing

Electricity flows everywhere inside our bodies. Our cells are specialized to conduct current through ions instead of electrons. The nervous system sends electrical signals throughout the body, enabling us to move, think, and feel. Internal electrical activities inside the body propagate through complex 3D conductive pathways and finally lead to spatiotemporally varying electrical potentials on the skin surface, which are called surface EP signals. Recording surface EP signals associated with, e.g., the brain, heart, and muscles enables health monitoring followed by early diagnosis of disorders and administration of chronic illnesses (1). EP sensing dates back to the eighteenth century (2). The emergence of soft electronics opened the door to soft wearable sensors that can measure, for example, EEG (3–9), ECG (7, 10-20), EMG (7, 14, 15, 21, 22), and electrooculogram (7, 23-26). EEG is widely used to diagnose encephalopathies such as stroke, brain tumor, schizophrenia, and epilepsy (27). Ultrathin (88-μm), large-area (8-channel), skull-conformable, and magnetic resonance imaging–compatible EEG sensors have been achieved through filamentary serpentine designs (28) (**Supplemental Figure 1*a***). A 500-nm-thick, transparent GET was applied as an imperceptible electrooculogram sensor around the human eye (29), which was successfully applied to control a drone through eye movement (23) (**Supplemental Figure 1*b***). ECG patterns are easy to recognize, and their changes in shape and periodicity are indicative of critical heart problems such as arrhythmia, myocardial infarction, and hypertension (30). Wireless and battery-free epidermal electronic systems have been placed on the chest of premature babies in neonatal intensive care units to monitor ECG on their delicate skin with no entanglement problems (31) (**Supplemental Figure 1*c***). EMG is available on any piece of muscle and is often used to detect neuromuscular abnormalities or control prostheses. A 16-channel, electrically compensated tattoo-like EMG sensor eliminated the need for interconnect encapsulation and was placed on the forearm of a left-hand amputee to control a prosthetic hand (104) (**Supplemental Figure 1*d***).

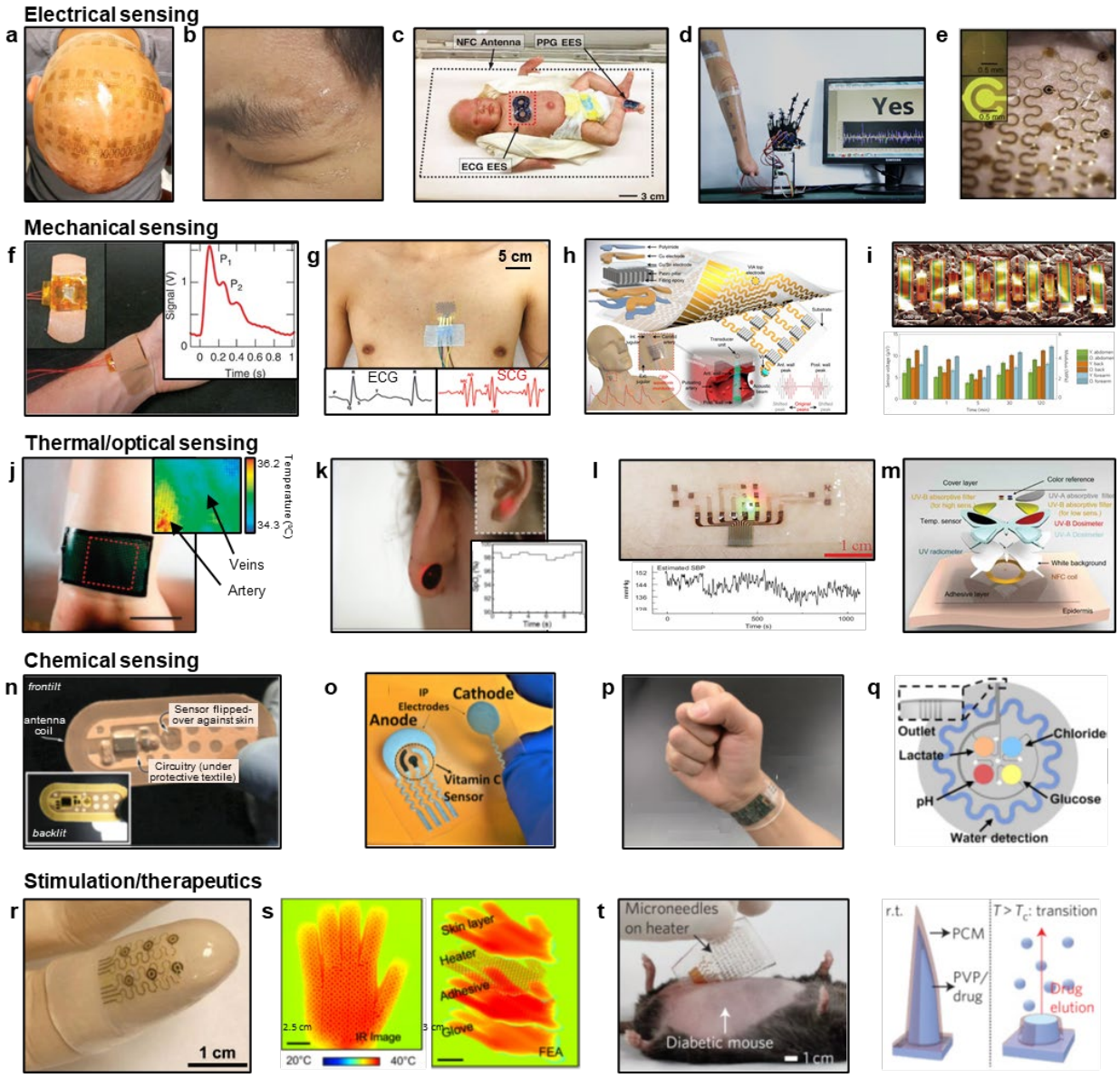

Supplemental Figure 1 Applications of wearable electronics as electrical, mechanical, thermal, optical, and chemical sensors or stimulators. (*a*) Ultrathin, large-area, skull conformable, and magnetic resonance imaging–compatible 8-channel electroencephalogram electrodes. Figure adapted with permission from reference (28); copyright 2019 Springer Nature. (*b*) Mechanically and optically imperceptible electrooculogram sensor based on transparent graphene e-tattoo. Figure adapted with permission from reference (23); copyright 2018 Springer Nature. (*c*) Wireless and battery-free epidermal ECG sensor on the chest of a premature baby. Figure adapted with permission from reference (31); copyright 2019 AAAS. (*d*) A 16-channel electrically compensated EMG sensor without needing to encapsulate the interconnects. Figure adapted with permission from reference (104); copyright 2020 AAAS. (*e*) Dot-ring-shaped epidermal hydration sensors. Figure adapted with permission from reference (32); copyright 2017 Springer Nature. (*f*) Optical image of organic-transistor-based ultrasensitive pressure sensor on arterial pulse (*left*) and

measured artery pulse waveform (*right*). Figure adapted with permission from reference (38); copyright 2013 Springer Nature. (*g*) Optical image of dual-mode chest e-tattoo (*left*) and synchronously measured ECG and SCG waveforms (*right*). Figure adapted with permission from reference (39); copyright 2019 Wiley-VCH. (*h*) Schematics of the stretchable and conformable ultrasonic transducer array for the measurement of arterial deformation and blood pressure. Figure adapted with permission from reference (40); copyright 2018 Springer Nature. (*i*) Scanning electron microscopy image of lead zinconate titanate–based thin, compliant skin modulus sensor (*top*) and in vivo measured skin modulus values for various skin locations (*bottom*). Figure adapted with permission from reference (41); copyright 2015 Springer Nature. (*j*) Optical image of soft temperature sensor on the wrist during occlusion (*left*) and measured spatial distributions of temperature (*right*). Figure adapted with permission from reference (47); copyright 2014 Springer Nature. (*k*) Optical image of a photoplethysmography sensor mounted on the back of earlobe (*right*) and measured SpO_2 (*left*). Figure adapted with permission from reference (57); copyright 2017 ACS. (*l*) Optical image of soft optoelectronic systems for cuff-less continuous blood pressure monitor (*top*) and the SBP monitored by the sensor (*bottom*). Figure adapted with permission from reference (58); copyright 2017 Wiley-VCH. (*m*) Exploded schematic illustration of a colorimetric UV dosimeter. Figure adapted with permission from reference (59); copyright 2020 Oxford University Press. (*n*) Photograph of an adhesive radio-frequency identification chemical sweat sensor. Figure adapted with permission from reference (65); copyright 2017 AAAS. (*o*) Optical image of a sweat vitamin C sensor. Figure adapted with permission from reference (66); copyright 2015 IEEE. (*p*) Photograph of a multiplexed wearable sweat sensor array integrated with a wireless printed circuit board. Figure adapted with permission from reference (68); copyright 2018 Wiley-VCH. (*q*) Schematic illustration of an epidermal colorimetric microfluidic sweat sensor. Figure adapted with permission from reference (69); copyright 2016 Springer Nature. (*r*) Optical image of electrotactile stimulator on a finger tube. Figure adapted with permission from reference (33); copyright 2012 IOP Publishing. (*s*) Infrared image (*left*) and finite element modeling results (*right*) for the heated hand by the e-glove system. Figure adapted with permission from reference (51); copyright 2019 Springer Nature. (*t*) Optical image of drug-loaded microneedles triggered by an integrated heater, which is laminated on the abdomen of a mouse (*left*) and schematic illustrations of the bioresorbable microneedles (*right*). Figure adapted with permission from reference (61); copyright 2018 Wiley-VCH. Abbreviation: ECG, electrocardiogram; EES, epidermal electronic systems; EMG, electromyogram; FEA, finite element analysis; IR, infrared; NFC, near-field communication; PCM, phase-change material; PPG; photoplethysmograms; PVP, polyvinyl pyrrolidone; SBP, systolic blood pressure; SCG, seismocardiography.

Skin-mounted electrodes could also be used to measure skin impedance, which correlates monotonically with skin hydration: The higher the hydration, the lower the impedance. Measuring and managing skin hydration is critical for preventing skin-based pathologies and regulating external appearance. Dot-ring-shaped hydration sensors have been widely used to measure localized hydration (32) (**Supplemental Figure 1*e***). Combined hydration and temperature mapping has enabled comprehensive electrothermal evaluation of skin health.

In addition to electrical sensing, the electrical stimulus to skin induces modulated electrical current into the tissue and excites cutaneous mechanoreceptors, allowing information to be

presented through the skin as an artificial touch sensation. Ying et al. (33) fabricated a 2 × 3 array of dot-ring-shaped electrodes inside a soft finger tube (**Supplemental Figure 1*r***). This array of electrotactile stimulators has been explored for programmable braille readers and displays for the visually impaired, as well as for individuals who suffer from vestibular disorders (34).

2. Mechanical signals

Skin is highly deformable. Hence, abundant mechanical signals are measurable on skin, associated with joint or muscle motion, the heartbeat on the chest, and pulses from shallow arteries. Many piezoresistive and piezocapacitive stretchable strain gauges have been developed for motion and gesture sensing (33, 35). Because they have already been reviewed extensively (36), we focus here on surface mechanical signals of biomedical significance. The arterial pulse is the most fundamental mechanophysiological signal in clinical medicine (37). Pulse wave analysis provides information on the stiffness and distensibility of an artery. Conventionally, pulse waves have been measured via tonometers, but nowadays, soft, wearable pressure sensors can provide mobile and continuous measurement. Pressure-sensitive, fast-response organic thin-film transistors were applied as high-fidelity pulse wave sensors over the radial artery (38) (**Supplemental Figure 1*f***). Another important mechanophysiological signal is seismocardiography (SCG), or chest vibration owing to mechanical events in the heartbeat, such as the opening and closing of heart valves. By combining filamentary serpentine gold electrodes and polymeric piezoelectric sensors on a stretchable e-tattoo, Ha et al. (39) could synchronously measure ECG and SCG (**Supplemental Figure 1*g***). Combining ECG and SCG peaks, multiple cardiac intervals, such as pre-ejection period and systole, could be extracted for each heartbeat from the dual-mode sensing. The linear correlation between systole and blood pressure (BP), which presented with the beat-by-beat systole measurement was demonstrated to be a viable means for beat-by-beat BP estimation. Arterial deformation deep inside the skin can be detected noninvasively using a soft array of ultrasonic transducers (40) (**Supplemental Figure 1*h***). Whereas conventional ultrasonic sensors suffer from unstable coupling with the human skin owing to the bulkiness and rigidity of the probes, the 4 × 5 ultrathin (200-μm) piezoelectric transducer array could fully conform to the skin and fully follow any subtle skin movement. At a working frequency of 7.5 MHz, the soft ultrasonic probe demonstrated an axial resolution of 400 μm, on par with state-of-the-art commercial ultrasonic probes. Therefore, it enabled central BP measurement over deeply embedded arteries at various body locations, such as the neck, arm, wrist, and foot.

In addition to cardiovascular health, mechanical sensing could be leveraged to assess the elastic modulus of skin in its natural condition. In vivo measurement of skin stiffness can provide insights into a variety of pathophysiological conditions; predict reactions to exogenous substances and environmental factors; help gauge the effectiveness of cosmetic products; and further establish mechanisms associated with growth, repair, and aging. Dagdeviren et al. (41) built a conformal modulus sensor, consisting of multiple pairs of piezoelectric actuators and transducers based on 500-nm-thick lead zinconate titanate for spatial mapping of the viscoelasticity of near-surface epidermis (**Supplemental Figure 1*i***). It could successfully detect skin stiffness variation at different body locations and after skin treatment.

3. Thermal/optical sensing

Body temperature is a key vital sign. Our thermoregulation system works hard to maintain our core body temperature around 36.5°C with a narrow variation (~1°C) (42). Irregular and abnormal changes in body temperature are a sign of certain illnesses accompanied by acute fever or hypothermia. Owing to the narrow range of acceptable body temperature, a major effort of wearable temperature sensors is to improve their temperature sensitivity and to achieve the mapping of subtle spatial variations of temperatures. Several mechanisms of temperature sensing have been introduced, such as thermistors (43, 44), thermocouples (thermoelectric effect) (45, 46), and colorimetry (47, 48). Thermistors and thermocouples are conventional temperature-sensing devices that detect changes in resistance and voltage, respectively, in response to temperature level. Colorimetry is used to improve spatial resolution, which is required for specific medical purposes, such as detecting breast cancers and other syndromes (49, 50). **Supplemental Figure 1*j*** shows soft temperature sensors exploiting thermochromic liquid crystals patterned into large-scale, pixelated arrays on thin elastomeric substrates (47). By using colorimetric temperature indicators, the temperature was visualized with milli-Kelvin precision (± 50 mK) and submillimeter spatial resolution. As a demonstration, measurements of temperature fluctuation above the ulnar artery were conducted as a part of reactive hyperemia. The temperature fluctuation owing to occlusion and release of blood flow was measured to be approximately 1.2 °C, which was comparable to the results from infrared cameras.

In addition to the thermal sensing, wearable bioelectronics could be applied to thermal therapy (**Supplemental Figure 1*s***) is a classic physiotherapy used in orthopedics to treat joint injuries that are often triggered by occupational overuse, obesity, or aging (51). Heat induces thermal expansion of the vascular systems and surrounding collagen tissues, relieving pain and reducing joint stiffness (52). To resolve the limitations of conventional thermal stimulators that cause discomfort to users, such as rigid stiffness and heavy weight, Choi et al. (53) created soft, wearable thermal stimulators for long-term, continuous, and comfortable articular thermotherapy. To make stretchable electrodes, a nanocomposite of AgNWs and thermoplastic elastomer was casted in a serpentine-patterned mold and encapsulated by a styrene–butadiene–styrene elastomer via heat pressing. The stretchable thermal stimulator could be stretched up to 100% and control the temperature up to 60°C in response to applied voltage and degree of stretch.

Although there is no illumination mechanism in our body, optical sensing is still very useful for long-term health monitoring. Photoplethysmography (PPG) is a measurement technique that detects the variation of light intensity when injected light passes through tissues and blood vessels. Blood volume changes owing to cardiovascular activity affect the intensity of the transmitted or reflected light, because the light-absorption rates of oxygenated and deoxygenated blood differ. PPG provides real-time monitoring of personal heart pulsation and blood oxygenation (54-57). **Supplemental Figure 1*k*** shows a soft PPG sensor on which two LEDs emit light of different wavelengths (red and infrared) into the earlobe (58). The reflected light is detected by two photodetectors on the same device, and this signal is called PPG. By analyzing light frequency and intensity, heart rate and blood oxygen saturation level could be monitored continuously. With the known distance between the two LEDs and the time delay in the two detected PPG signals, pulse

wave velocity could be extracted (59) (**Supplemental Figure 1*l***). According to the well-known relationship between pulse wave velocity and BP, continuous BP could be estimated via the noninvasive PPG device.

Solar radiation through UV light is a leading cause of skin disease. Therefore, a quantitative, wearable UV dosimeter has been built based on colorimetry (60) (**Supplemental Figure 1*m***). The colorimetric chemistry uses (4-phenoxyphenyl)diphenylsulfonium triflate with crystal violet lactone and Congo red for UV-A and UV-B operation, respectively, when integrated with suitable optical filters. L′Oréal has successfully commercialized this technology to demonstrate the effectiveness of their sunscreens for their customers.

4. Chemical sensing

The aforementioned electrical, mechanical, thermal, and optical sensors all measure physical signals from the body. However, our body is full of chemical biomarkers (metabolites) that are very direct indicators of, e.g., diseases, stress levels, and drug usage (59, 60). The current gold standard for chemical biomarker analysis is blood work. But a blood test is painful and unable to offer continuous and long-term monitoring. In contrast, eccrine sweat is a readily available, noninvasive biofluid for the continuous assessment of analytes in our body (63). Prior to wearable sweat sensors, collecting sweat and quantifiably monitoring sweat rate could be used to assess stress levels and/or prevent dehydration (64). With the development of sweat uptake materials and sweat stimulation techniques (e.g., iontophoresis) (65), wearable, continuous sweat sensors could be built. Withdrawn sweat is electrochemically analyzed to monitor useful biomarkers, such as nutrition state, sweat metabolites, and electrolytes. Rose et al. (66) fabricated a soft adhesive sweat sensor that can measure sodium ion concentration (**Supplemental Figure 1*n***). A triple-printed ionophore membrane established a difference in potential across the electrode–ionophore barrier corresponding to sodium ion concentration, enabling a simple potentiometric measurement. The measured data were transferred to mobile devices through RF identification.

Aiming to provide guidance on personalized nutrition, Sempionatto et al. (67) invented a chemical sweat sensor to detect variations in vitamin levels (**Supplemental Figure 1*o***). Vitamin C in sweat was detected by immobilizing the enzyme ascorbate oxidase on flexible tattoo electrodes and monitoring changes in the reduction current of the oxygen cosubstrate. Because the enzyme biosensor had a highly selective response, a dynamic rise and fall in vitamin C sweat levels after the intake of vitamin C pills and fruit juices was demonstrated with no interference from other sweat constituents.

To simultaneously measure multiple metabolites and electrolytes, Hong et al. (68) created integrated sweat sensors capable of multiplexed screening of target biomarkers. Gao et al. (69) fabricated smart wristbands that could measure sweat metabolites (glucose and lactate) and electrolytes (sodium and potassium ions) (**Supplemental Figure 1*p***). The IC in the wristband conducted all data processes for real-time assessment of participants' physiological states.

Leveraging soft microfluidics, Koh et al. (70) fabricated a sweat sensor that not only detected glucose, lactate, pH, and chloride but also directly measured sweat rate (**Supplemental Figure 1*g***). The soft microfluidic system harvested sweat through pores and routed the sweat to different channels and reservoirs. Embedded chemical analyses responded in colorimetric fashion to the biomarkers that were subsequently quantified by wireless digital image capture hardware. Human studies validated the sweat sensor's functionality during long-distance bicycle racing (104 km) in arid, outdoor conditions.

In addition to chemical sensing, soft wearable devices could also function as chemical stimulators in, for example, drug delivery systems (71). Lee et al. (62) fabricated a soft and wireless wristband for smart and wireless administration of medications (**Supplemental Figure 1*t***). Glucose level was monitored via a chemical sweat sensor, and detection of hyperglycemia triggered the degradation of the drug-loaded microneedles. A thermally active bioresorbable coating layer of a phase-change material over the microneedles protected the drug and bioresorbable polymer (polyvinyl pyrrolidone) from moisture and/or biofluids. Thermal actuation above the critical temperature (41°C) molted the phase-change material and released drug into the bloodstream. The sequential heating triggered the drug release in a stepwise manner, and the number of drug deliveries was decided by the total area of the microneedles.

Supplemental Appendix 2

Implantable-Type Applications of Soft Bioelectronics

The brain, spine, and heart are representative target organs for such applications (72). Among these organs, particular attention has been given to the brain. Various efforts have been made to record and modulate EP signals on the brain. EP signals recorded directly from the brain, such as signals of ECoG and intracortical encephalography, are useful to understand neural activities and pathologies. The amplitude (10 μV~10 mV) and spatiotemporal resolution (~100 μm, 30 ms) of the signal from implanted neural probes are much higher than those from surface encephalography electrodes (5~300 μV, ~10 mm, 50 ms), because the amplitude of EP signals decreases while the signal passes through tissue layers such as the dura mater, skull, and scalp. Therefore, various implantable-type soft bioelectronic devices have been developed for brain research.

A stretchable nanocomposite that consists of gold-coated titanium dioxide nanowires with PDMS encapsulation was applied for ECoG measurement. The device had 32 electrodes with a pitch of 200 μm and a thickness of ~80 μm (73). The conductivity of the stretchable composite was 16,000 S/cm, which could be maintained during repetitive stretching tests (1,000 cycles with an applied strain of 100%). The nanocomposite electrode was mounted on the cortex of a rat to record somatosensory evoked potentials (SSEPs) (**Supplemental Figure 2*a***). Owing to the high elasticity of the material, the electrode could make conformal contact on the pial cortical surface (**Supplemental Figure 2*b***). The electrode could be implanted for 3 months and record SSEP from a freely moving animal (**Supplemental Figure 2*c***). The recording of SSEP, which is responsive to hind-limb stimulation, was also demonstrated (**Supplemental Figure 2*d***). The electrode could also record the local field potential for sleep epochs, including rapid and nonrapid eye movement epochs.

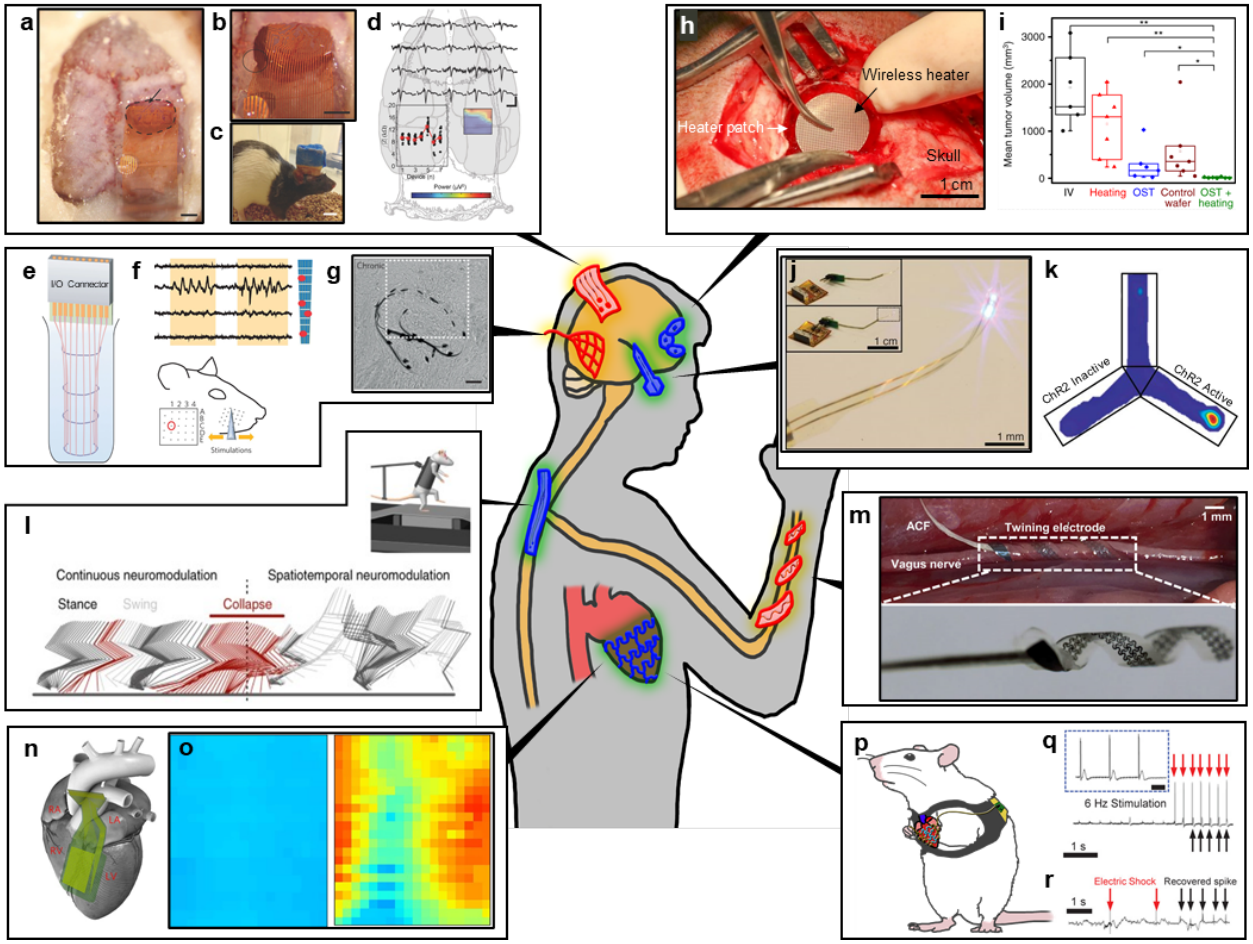

Supplemental Figure 2 Applications of implantable electronics on brain and nervous system and the heart. (*a–c*) Optical images of a metallic nanocomposite multichannel electrode implanted on a freely moving rat brain. (*d*) A somatosensory evoked potentials recording with a metallic nanocomposite multichannel electrode. (*a-d*) Figure adapted with permission from reference (73); Copyright 2018. Wiley-VCH. (*e*) Schematic illustration of 3D microporous electronics soaked in a beaker. (*f*) The probe recorded somatosensory cortex signal response to whisker stimulation. (*g*) Microscopy image of the recovered brain tissue recovered 5 weeks after implantation. (*e-g*) Figure adapted with permission from reference (74); copyright 2015 Springer Nature. (*h*) Optical image of a BEP implanted in canine model brain. (*i*) Tumor volume differences between BEP implanted groups and control groups. (*h,i*) Figure adapted with permission from reference (75); copyright 20195 Springer Nature. (*j*) Optical image of the brain implantable optical stimulator with μ-ILED. Inset image shows integration with the wireless module. (*k*) A Y-maze test after modulation of animal behavior via optogenetic stimulation. (*j,k*) Figure adapted with permission from reference (76); Copyright 2013, AAAS. (*l*) Experimental schematics of a locomotion test of rats during spinal stimulation [*top* (77)] and spatiotemporal stimulation result [*bottom* (78)]. Figure adapted with permission from reference (77); Copyright 2015, AAAS. Figure adapted with permission from reference (78); Copyright 2016, Springer Nature. (*m*) Optical image of twining electrodes on the vagus nerve in vivo (*top*) and in vitro (*bottom*). Figure adapted with permission from reference (79); Copyright 2019, AAAS. (*n*) Schematic illustration of the 396-channel cardiac ECG sensor

on the heart. (*o*) Time-dependent 2D ECG mapping on an extracted heart. (*n,o*) Figure adapted with permission from reference (82); Copyright 2017, Springer Nature. (*p*) Schematic illustration of a rat with epicardial mesh electronics. (*q,r*) ECG data of cardiac stimulation results with epicardial mesh electronics. (*q*) Beat-rate modulation and (*r*) defibrillation. (*p-r*) Figure adapted with permission from reference (85); Copyright 2019. Wiley-VCH. Abbreviations: μ-ILED, micro-inorganic light-emitting diode; ACF; anisotropic conductive film; BEP, bioresorbable electronic patch; ECG, electrocardiogram; OST, oxidized starch.

As briefly introduced in the Section 2.3, 3D macroporous electronics have been applied to intracortical encephalography (74). Ultrathin (~10-μm) mesh electrodes, whose open space is 80% of the entire device area, feature high flexibility with a bending stiffness of ~0.64×10^{-15} N/m^2. The transverse compressive strain and local tensile strain induced on the mesh electrode led to a cylindrical probe structure with sensor arms bent away from the cylinder (**Supplemental Figure 2*e***). The probe was implanted into the somatosensory cortex of a rat and could record signals with high amplitudes (~6.3 ± 0.4 mV), which corresponded to whisker C1 stimulation (**Supplemental Figure 2*f***). At 5 weeks after implantation, the void induced during implantation was not visible, indicating that the brain tissue filled the space of the 3D macroporous structure. Bright-field microscopy images showed a high density of neuron cells near the macroporous probe (~50 μm proximity) (**Supplemental Figure 2*g***).

Conventional drug delivery strategies, such as oral administration or intravenous injection, have drawbacks, particularly for drug delivery to the brain: (*a*) Spatiotemporal control of the delivery is difficult, (*b*) drugs are delivered to unintended organs, and (*c*) drugs cannot interpenetrate the blood–brain barrier. Recently, Lee et al. (75) introduced the bioresorbable electronic patch (BEP), a flexible, sticky, biodegradable, and wirelessly controlled device to deliver drugs intracortically while bypassing the blood–brain barrier (**Supplemental Figure 2*h***). A wireless temperature sensor and a wireless heater, fabricated with biodegradable materials such as ultrathin poly(lactic acid), poly(lactic-coglycolic acid), and Mg, were integrated with a biodegradable drug reservoir made of oxidized starch containing 6.831 mg of a chemotherapy drug (doxorubicin). The BEP showed strong adhesion (~80 kPa shear stress) to the brain tissue, which allowed drug delivery to be localized in the contacted region of the brain. The drug delivery could be accelerated by wireless mild-thermic actuation. An external coil generated RF magnetic fields, which triggered eddy current and Joule heating in the heater of the BEP. The raised temperature (~42°C) accelerated drug diffusion. The BEP-implanted group showed a significantly reduced tumor volume (**Supplemental Figure 2*i***) and higher survival rate compared with control groups.

Optogenetics have been studied as a novel strategy to modulate a single group of neurons in a highly specific manner. The targeted neuron was intentionally infected with a gene-modified virus sensitive to a specific wavelength of light and then stimulated and/or inhibited by light delivery. Thus, soft, implantable light-delivering devices have been developed for optogenetics. For example, flexible bioelectronics, including a microinorganic-LED (μ-ILED), a microelectrode, an inorganic photodetector, and a temperature sensor, have been developed (76). The ultrasmall μ-ILED (6.45 μm thick, 50 × 50 μm^2 lateral dimensions) was mounted on an ultrathin (~500 nm) epoxy layer (**Supplemental Figure 2*j***). The bioelectrode with the μ-ILED was implanted on the

ventral tegmental area, which included dopaminergic neurons preinfected with the light-sensitive virus. The μ-ILED was controlled wirelessly, which enabled long-term optical stimulations. In the Y maze test, light stimulations (205-ms pulses for every nose poke) were applied to the dopamine reward pathway of mice (**Supplemental Figure 2*k***). The stimulated mice showed a significantly higher number of nose poking trials than control groups, indicating that the light delivery successfully controlled animal behavior.

In addition to the brain, the spine and peripheral nerves are important targets for treatment using soft bioelectronics. Electrical stimulations on the spinal cord and peripheral nerves have been a useful tool for releasing chronic pain. Minev et al. (77) proposed an electronic dura mater, in which thin gold films are patterned on a silicone elastomer. The electronic dura mater was implanted in the injured spine of a rat to restore locomotion (**Supplemental Figure 2*l***). The electrical stimulation (40 Hz, 0.2 ms, 50~150 μA) on the lateral aspect of the L2 and S1 segments enabled the paralyzed rat to walk. In following work, the same researchers developed stimulation protocols to mimic natural locomotion dynamics (78). The stimulation pattern could be controlled spatially in real time to modulate extensor versus flexor movement of the muscle. The spatiotemporal modulation improved gait quality, and the result showed that sophisticated control protocols to treat paralysis could be established via cooperation between engineers and clinicians.

The vagus, or pneumogastric, nerve is an essential peripheral nerve, which interfaces signals for parasympathetic control of the heart, lung, and digestive tract. The aforementioned self-deformable electrode was applied to the rabbit vagus nerve to record signals and perform stimulations (VNS; vagus nerve stimulations) (79). Twining electrodes with an inner diameter of 1 mm were implanted on the rabbit vagus nerve (**Supplemental Figure 2*m***). The shape-memory polymer responded to the rabbit's body temperature, and the twining process was proceeded on the rabbit nerve by its self-deforming in vivo. A rabbit model of heart failure was prepared for further demonstrations. The heart rate increased dramatically (to 240 bpm) and then went into an autonomic dysfunction state after injection of epinephrine. After VNS (0.4 mA, 10 Hz, and 0.1-ms pulse) by the twining electrode, the elevated heart rate was returned to a normal state.

The heart is another critical organ controlled by electrical signals (80). The downstream neural signal evoked from the brain controls activation of the sinoatrial node. This node generates rhythmical pulses that flow along with the cardiac conduction system. Typically, cardiac conduction has been monitored by surface ECG and/or lead ECG, which cannot represent local ECG of the specific heart region. Recently, soft electronics have been introduced that can record ECG on the surface of the dynamically beating heart without interrupting the original heart motion (81). For example, Fang et al. (82) reported a 396-channel multiplexed electrode array based on ultrathin transistors, which successfully recorded high-density ECG signals on a rabbit heart (**Supplemental Figure 2*n***). Owing to their high flexibility, the multichannel electrodes could make conformal contact on the beating heart. As a result, a 2D map showing time-dependent cardiac electrophysiology changes could be produced (**Supplemental Figure 2*o***). Further systematic studies were performed to understand propagation of local ECG signals under normal, paced, and arrhythmic heart conditions.

In another example, a stretchable epicardial mesh was applied to the rat heart to record ECG and modulate heartbeat (83). The mesh was fabricated with a stretchable nanocomposite consisting of AgNWs and an elastomer. The percolation network of AgNWs inside the elastomeric matrix allowed high conductivity. The serpentine-shaped epicardial mesh showed softness similar to that of cardiac muscle. The mesh successfully recorded ECG on the beating heart. To remove potential toxicity from silver, a gold sheath was added to AgNWs (i.e., Au@AgNWs) in subsequent work (84). Au@AgNWs showed high biocompatibility without losing high conductivity (41,850 S/cm). According to inductively coupled plasma mass spectrometry analysis, there was no meaningful cytotoxic response by the Au@AgNW nanocomposite implanted into mice for 3 weeks. A 34-channel electrode array was fabricated with the Au@AgNW nanocomposite and implanted on a swine heart. The electrode successfully recorded ECG and modulated the swine heart in vivo. More recently, Pt black was added to the Au@AgNW nanocomposite (85). Pt black significantly reduced nanocomposite impedance. The resulting epicardial mesh successfully recorded ECG with a high SNR from a rat in vivo (**Supplemental Figure 2*p***). Also, it could modulate abnormal heart activities, such as bradycardia (**Supplemental Figure 2*q***) and ventricular fibrillation (**Supplemental Figure 2*r***). These results demonstrate the potential of epicardial mesh for cardiac resynchronization and defibrillation.

Supplemental Table 1 Mechanical and electrochemical properties of the materials introduced in the review

Materials \ Properties		Mechanical property		Electrochemical property				Reference
		Stretchability	Young's modulus	Conductivity	Impedance	Charge storage capacity	Charge injection limit	
Liquid metal		15%		3,400,000 S/m				86
			1.055 MPa	4 Ω	4.5 Ω			87
			1 MPa	3,703,700 S/m	6.74 kΩ	4.5 mC/cm^2		88
Conductive material on soft substrate	Nanomaterial coating on soft material	100%		6.12 Ω				89
		100%		200 Ω				90
	Electrically conductive fabric	10%	36.5 MPa	15,390 S/m				91
		25%		0.15 Ω/cm				92
Conductive Polymer	PEDOT:PSS				2,000 Ω	2.71 mC/cm^2	1.9 mC/cm^2	93
		100%	1,000 Mpa	410,000 S/m	5 Ω			94
Hydrogel composite	Conductive polymer	20%	30 kPa	5,000 S/m	1,000 Ω	164 mC/cm^2		95
		35%	2 Mpa	0.4 S/m		60 mC/cm^2	8.3 mC/cm^2	96
	Carbon nanomaterial	400%	18.2 kPa	15.3 S/m	20 Ω			97
			1.5 kPa	0.1345 S/m	50 kΩ			98
	Metallic nanomaterial	30%	15.5 MPa	18.6 Ω/cm	20 Ω			99
Elastomeric composite	Carbon nanomaterial	148%	8.94 MPa	0.88 S/m	529 Ω			100
		100%	2.7 MPa	0.01 S/cm	100 Ω			101
	Metallic nanomaterial	400%		400,000 S/m				102
		90%		1,121,000 S/m				82
		840%	3.28 MPa	4,185,000 S/m	800 Ω			83
		720%		2,950,000 S/m	70 Ω	25 mC/cm^2	5.12 mc/cm^2	84
	Metal doping	130%		12,000,000 S/m	120 Ω			103

Supplemental Table 2 Representative advantages and disadvantages of the novel material introduced in this review

Materials		Pros	Cons
Liquid metal		High conductivity High softness Almost infinite stretchability	Poor interfacial property Must be encapsulated in channel, leakage issue Controversial biocompatibility Complicated fabrication process
Conductive material on soft substrate	Nanomaterial coating on soft material	Cost-efficient fabrication	Low strechability Weak mechanical robustness
	Electrically conductive fabric	High breathability Good processability	Low softness Poor interfacial property Poor conformal contact
Conductive polymer		High electrochemical property Facile fabrication (solution processable)	Poor electric conductivity High elastic modulus
Hydrogel composite	Conductive polymer	High electrochemical property High softness High biocompatibility	Low electric conductivity Low stability in air (drying)
	Carbon nanomaterial	High softness Good strechability	Poor electric conductivity Low stability in air (drying)
	Metallic nanomaterial	High softness Good electric conductivity	Poor processability Low stability in air (drying)
Elastomeric composite	Carbon nanomaterial	Good electrochemical property	Poor electric conductivity
	Metallic nanomaterial	High electric conductivity High strechability	Poor interfacial property
	Metal doping	High electrical conductivity	Low processability

Reference

1. Ha M, Lim S, Ko H. 2018. Wearable and flexible sensors for user-interactive health-monitoring devices. *J. Mater. Chem. B* 6(24):4043–64
2. Verkhratsky A, Parpura V. 2014. History of electrophysiology and the patch clamp. Methods Mol. Biol. 1183:1–19
3. Xu S, Zhang Y, Jia L, Mathewson KE, Jang K-I, et al. 2014. Soft microfluidic assemblies of sensors, circuits, and radios for the skin. *Science* 344(6179):70–74
4. Jeong J-W, Kim MK, Cheng H, Yeo W-H, Huang X, et al. 2014. Capacitive epidermal electronics for electrically safe, long-term electrophysiological measurements. *Adv. Healthc. Mater.* 3(5):642–48
5. Kuzum D, Takano H, Shim E, Reed JC, Juul H, et al. 2014. Transparent and flexible low noise graphene electrodes for simultaneous electrophysiology and neuroimaging. *Nat. Commun.* 5:5259

6. Lu N, Yang S, Wang P. 2016. “Cut-and-paste” manufacture of multiparametric epidermal electronic systems. *Adv. Mater.* 27(41):6423–30
7. Jang K-I, Jung HN, Lee JW, Xu S, Liu YH, et al. 2016. Ferromagnetic, folded electrode composite as a soft interface to the skin for long-term electrophysiological recording. *Adv. Funct. Mater.* 26(40):7281–90
8. Debener S, Emkes R, De Vos M, Bleichner M. 2015. Unobtrusive ambulatory EEG using a smartphone and flexible printed electrodes around the ear. *Sci. Rep.* 5:16743
9. Goverdovsky V, von Rosenberg W, Nakamura T, Looney D, Sharp DJ, et al. 2017. Hearables: multimodal physiological in-ear sensing. *Sci. Rep.* 7:6948
10. Xu S, Zhang Y, Jia L, Mathewson KE, Jang K-I, et al. 2014. Soft microfluidic assemblies of sensors, circuits, and radios for the skin. *Science* 344(6179):70–74
11. Jang K-I, Chung HU, Xu S, Lee CH, Luan H, et al. 2015. Soft network composite materials with deterministic and bio-inspired designs. *Nat. Commun.* 6:6566
12. Kim D-H, Lu N, Ghaffari R, Kim Y-S, Lee SP, et al. 2011. Materials for multifunctional balloon catheters with capabilities in cardiac electrophysiological mapping and ablation therapy. *Nat. Mater.* 10(4):316–23
13. Yamamoto Y, Yamamoto D, Takada M, Naito H, Arie T, et al. 2017. Efficient skin temperature sensor and stable gel-less sticky ECG sensor for a wearable flexible healthcare patch. *Adv. Healthc. Mater.* 6(17):1700495
14. Lu N, Yang S, Wang P. 2016. “Cut-and-paste” manufacture of multiparametric epidermal electronic systems. *Adv. Mater.* 27(41):6423–30
15. Han S, Kim MK, Wang B, Wie DS, Wang S, Lee CH. 2016. Mechanically reinforced skin-electronics with networked nanocomposite elastomer. *Adv. Mater.* 28(46):10257–65
16. Hwang S-W, Lee CH, Cheng H, Jeong J-W, Kang S-K, et al. 2015. Biodegradable elastomers and silicon nanomembranes/nanoribbons for stretchable, transient electronics, and biosensors. *Nano Lett.* 15(5):2801–8
17. Kim D-H, Ghaffari R, Lu N, Wang S, Lee SP, et al. 2012. Electronic sensor and actuator webs for large-area complex geometry cardiac mapping and therapy. *PNAS* 109(49):19910–15
18. Kim DH, Lu N, Ma R, Kim YS, Kim RH, et al. 2011. Epidermal electronics. *Science* 333(6044):838–43

19. Khan Y, Garg M, Gui Q, Schadt M, Gaikwad A, et al. 2016. Flexible hybrid electronics: direct interfacing of soft and hard electronics for wearable health monitoring. *Adv. Funct. Mater.* 26(47):8764–75
20. Koo JH, Jeong S, Shim HJ, Son D, Kim J, et al. 2017. Wearable electrocardiogram monitor using carbon nanotube electronics and color-tunable organic light-emitting diodes. *ACS Nano* 11(10):10032–41
21. Xu S, Zhang Y, Jia L, Mathewson KE, Jang K-I, et al. 2014. Soft microfluidic assemblies of sensors, circuits, and radios for the skin. *Science* 344(6179):70–74
22. Roberts T, De Graaf JB, Nicol C, Hervé T, Fiocchi M, Sanaur S. 2016. Flexible inkjet-printed multielectrode arrays for neuromuscular cartography. *Adv. Healthc. Mater.* 5(12):1462–70
23. Ameri SK, Kim M, Kuang IA, Perera WK, Alshiekh M, et al. 2018. Imperceptible electrooculography graphene sensor system for human-robot interface. *npj 2D Mater. Appl.* 2:19
24. Vidal M, Turner J, Bulling A, Gellersen H. 2012. Wearable eye tracking for mental health monitoring. *Comput. Commun.* 35(11):1306–11
25. Heo J, Yoon H, Park K. 2017. A novel wearable forehead EOG measurement system for human computer interfaces. *Sensors* 17(7):1485
26. Paul GM, Fan Cao, Torah R, Kai Yang, Beeby S, Tudor J. 2014. A smart textile based facial EMG and EOG computer interface. *IEEE Sens. J.* 14(2):393–400
27. Kaplan PW, Rossetti AO. 2011. EEG patterns and imaging correlations in encephalopathy. *J. Clin. Neurophysiol.* 28(3):233–51
28. Tian L, Zimmerman B, Akhtar A, Yu KJ, Moore M, et al. 2019. Large-area MRI-compatible epidermal electronic interfaces for prosthetic control and cognitive monitoring. *Nat. Biomed. Eng.* 3(3):194–205
29. Choi C, Choi MK, Liu S, Kim MS, Park OK, et al. 2017. Human eye-inspired soft optoelectronic device using high-density MoS_2-graphene curved image sensor array. *Nat. Commun.* 8:1664
30. De Bacquer D, De Backer G, Kornitzer M, Blackburn H. 1998. Prognostic value of ECG findings for total, cardiovascular disease, and coronary heart disease death in men and women. *Heart* 80(6):570–77

31. Chung HU, Kim BH, Lee JY, Lee J, Xie Z, et al. 2019. Binodal, wireless epidermal electronic systems with in-sensor analytics for neonatal intensive care. *Science* 363(6430):eaau0780
32. Krishnan S, Shi Y, Webb RC, Ma Y, Bastien P, et al. 2017. Multimodal epidermal devices for hydration monitoring. *Microsyst. Nanoeng.* 3:17014
33. Ying M, Bonifas AP, Lu N, Su Y, Li R, et al. 2012. Silicon nanomembranes for fingertip electronics. *Nanotechnology* 23(34):344004
34. Danilov YP, Tyler ME, Kaczmarek KA. 2008. Electrotactile vision: achievements, problems and perspective. *Int. J. Psychophysiol.* 69(3):162–63
35. Lu N, Lu C, Yang S, Rogers J. 2012. Highly sensitive skin-mountable strain gauges based entirely on elastomers. *Adv. Funct. Mater.* 22(19):4044–50
36. Souri H, Banerjee H, Jusufi A, Radacsi N, Stokes AA, et al. 2020. Wearable and stretchable strain sensors: materials, sensing mechanisms, and applications. *Adv. Intell. Syst.* 2(8):e2000039
37. Song J-K, Son D, Kim J, Yoo YJ, Lee GJ, et al. 2017. Wearable force touch sensor array using a flexible and transparent electrode. *Adv. Funct. Mater.* 27(6):1605286
38. Schwartz G, Tee BC-K, Mei J, Appleton AL, Kim DH, et al. 2013. Flexible polymer transistors with high pressure sensitivity for application in electronic skin and health monitoring. *Nat. Commun.* 4:1859
39. Ha T, Tran J, Liu S, Jang H, Jeong H, et al. 2019. A chest-laminated ultrathin and stretchable e-tattoo for the measurement of electrocardiogram, seismocardiogram, and cardiac time intervals. *Adv. Sci.* 6(14):1900290
40. Wang C, Li X, Hu H, Zhang L, Huang Z, et al. 2018. Monitoring of the central blood pressure waveform via a conformal ultrasonic device. *Nat. Biomed. Eng.* 2(9):687–95
41. Dagdeviren C, Shi Y, Joe P, Ghaffari R, Balooch G, et al. 2015. Conformal piezoelectric systems for clinical and experimental characterization of soft tissue biomechanics. *Nat. Mater.* 14(7):728–36
42. Lim CL, Byrne C, Lee JKW. 2008. Human thermoregulation and measurement of body temperature in exercise and clinical settings. *Ann. Acad. Med.* 37(4):347–53
43. Ren X, Pei K, Peng B, Zhang Z, Wang Z, et al. 2016. A low-operating-power and flexible active-matrix organic-transistor temperature-sensor array. *Adv. Mater.* 28(24):4832–38

44. Salvatore GA, Sülzle J, Dalla Valle F, Cantarella G, Robotti F, et al. 2017. Biodegradable and highly deformable temperature sensors for the internet of things. *Adv. Funct. Mater.* 27(35):1702390
45. Zhang F, Zang Y, Huang D, Di C, Zhu D. 2015. Flexible and self-powered temperature-pressure dual-parameter sensors using microstructure-frame-supported organic thermoelectric materials. *Nat. Commun.* 6:8356
46. Imran M, Bhattacharyya A. 2006. Effect of thin film thicknesses and materials on the response of RTDs and microthermocouples. *IEEE Sens. J.* 6(6):1459–67
47. Gao L, Zhang Y, Malyarchuk V, Jia L, Jang K-I, et al. 2014. Epidermal photonic devices for quantitative imaging of temperature and thermal transport characteristics of the skin. *Nat. Commun.* 5:4938
48. Zang X, Wang X, Jiang Y, Wang X, Yang Z, et al. 2017. Conducting polymer based visual-aided smart thermosensors on arbitrary substrates. *Adv. Funct. Mater.* 27(41):1702706
49. Arora N, Martins D, Ruggerio D, Tousimis E, Swistel AJ, et al. 2008. Effectiveness of a noninvasive digital infrared thermal imaging system in the detection of breast cancer. *Am. J. Surg.* 196(4):523–26
50. Kennedy DA, Lee T, Seely D. 2009. A comparative review of thermography as a breast cancer screening technique. *Integr. Cancer Ther.* 8(1):9–16
51. Kim M, Parasuraman R, Wang L, et al. 2019. Soft-packaged sensory glove system for human-like natural interaction and control of prosthetic hands. *NPG Asia Mater*. 11:43
52. Brosseau L, Yonge K, Welch V, Marchand S, Judd M, et al. 2003. Thermotherapy for treatment of osteoarthritis. *Cochrane Database Syst. Rev.* 2003(4):cd004522
53. Choi S, Park J, Hyun W, Kim J, Kim J, et al. 2015. Stretchable heater using ligand-exchanged silver nanowire nanocomposite for wearable articular thermotherapy. *ACS Nano* 9(6):6626–33
54. Xu H, Liu J, Zhang J, Zhou G, Luo N, Zhao N. 2017. Flexible organic/inorganic hybrid near-infrared photoplethysmogram sensor for cardiovascular monitoring. *Adv. Mater.* 29(31):1700975
55. Yokota T, Zalar P, Kaltenbrunner M, Jinno H, Matsuhisa N, et al. 2016. Ultraflexible organic photonic skin. *Sci. Adv.* 2(4):e1501856
56. Lochner CM, Khan Y, Pierre A, Arias AC. 2014. All-organic optoelectronic sensor for pulse

oximetry. *Nat. Commun.* 5:5745

57. Kim T-H, Lee C-S, Kim S, Hur J, Lee S, et al. 2017. Fully stretchable optoelectronic sensors based on colloidal quantum dots for sensing photoplethysmographic signals. *ACS Nano* 11(6):5992–6003
58. Kim J, Gutruf P, Chiarelli AM, Heo SY, Cho K, et al. 2017. Miniaturized battery-free wireless systems for wearable pulse oximetry. *Adv. Funct. Mater.* 27(1):1604373
59. Li H, Ma Y, Liang Z, Wang Z, Cao Y, et al. 2020. Wearable skin-like optoelectronic systems with suppression of motion artifacts for cuff-less continuous blood pressure monitor. *Natl. Sci. Rev.* 7(5):849–62
60. Araki H, Kim J, Zhang S, Banks A, Crawford KE, et al. 2017. Materials and device designs for an epidermal UV colorimetric dosimeter with near field communication capabilities. *Adv. Funct. Mater.* 27(2):1604465
61. Lee H, Hong YJ, Baik S, Hyeon T, Kim D. 2018. Enzyme-based glucose sensor: from invasive to wearable device. *Adv. Healthc Mater.* 7(8):1701150
62. Lee H, Choi TK, Lee YB, Cho HR, Ghaffari R, et al. 2016. A graphene-based electrochemical device with thermoresponsive microneedles for diabetes monitoring and therapy. *Nat. Nanotechnol.* 11(6):566–72
63. Heikenfeld J, Jajack A, Feldman B, Granger SW, Gaitonde S, et al. 2019. Accessing analytes in biofluids for peripheral biochemical monitoring. *Nat. Biotechnol.* 37(4):407–19
64. Zhao FJ, Bonmarin M, Chen ZC, Larson M, Fay D, et al. 2020. Ultra-simple wearable local sweat volume monitoring patch based on swellable hydrogels. *Lab Chip* 20:168–74
65. Chen Y, Lu S, Zhang S, Li Y, Qu Z, et al. 2017. Skin-like biosensor system via electrochemical channels for noninvasive blood glucose monitoring. *Sci. Adv.* 3(12):e1701629
66. Rose DP, Ratterman ME, Griffin DK, Hou L, Kelley-Loughnane N, et al. 2015. Adhesive RFID sensor patch for monitoring of sweat electrolytes. *IEEE Trans. Biomed. Eng.* 62(6):1457–65
67. Sempionatto JR, Khorshed AA, Ahmed A, De Loyola e Silva AN, Barfidokht A, et al. 2020. Epidermal enzymatic biosensors for sweat vitamin C: toward personalized nutrition. *ACS Sensors* 5(6):1804–13
68. Hong YJ, Lee H, Kim J, Lee M, Choi HJ, et al. 2018. Multifunctional wearable system that

integrates sweat-based sensing and vital-sign monitoring to estimate pre-/post-exercise glucose levels. *Adv. Funct. Mater.* 28(47):1805754

69. Gao W, Emaminejad S, Nyein HYY, Challa S, Chen K, et al. 2016. Fully integrated wearable sensor arrays for multiplexed *in situ* perspiration analysis. *Nature* 529(7587):509–14
70. Koh A, Kang D, Xue Y, Lee S, Pielak RM, et al. 2016. A soft, wearable microfluidic device for the capture, storage, and colorimetric sensing of sweat. *Sci. Transl. Med.* 8(366):366ra165
71. Lee H, Song C, Baik S, Kim D, Hyeon T, Kim D-H. 2018. Device-assisted transdermal drug delivery. *Adv. Drug Deliv. Rev.* 127:35–45
72. Lee M, Shim HJ, Choi C, Kim DH. 2019. Soft high-resolution neural interfacing probes: materials and design approaches. *Nano Lett.* 19(5):2741–49
73. Tybrandt K, Khodagholy D, Dielacher B, Stauffer F, Renz AF, et al. 2018. High-density stretchable electrode grids for chronic neural recording. *Adv. Mater.* 30(15):1706520
74. Xie C, Liu J, Fu TM, Dai X, Zhou W, Lieber CM. 2015. Three-dimensional macroporous nanoelectronic networks as minimally invasive brain probes. *Nat. Mater.* 14(12):1286–92
75. Lee J, Cho HR, Cha GD, Seo H, Lee S, et al. 2019. Flexible, sticky, and biodegradable wireless device for drug delivery to brain tumors. *Nat. Commun.* 10:5205
76. Kim T-i, McCall JG, Jung YH, Huang X, Siuda ER, et al. 2013. Injectable, cellular-scale optoelectronics with applications for wireless optogenetics. *Science* 340(6129):211–16
77. Minev IR, Musienko P, Hirsch A, Barraud Q, Wenger N, et al. 2015. Electronic dura mater for long-term multimodal neural interfaces. *Science* 347(6218):159–63
78. Wenger N, Moraud EM, Gandar J, Musienko P, Capogrosso M, et al. 2016. Spatiotemporal neuromodulation therapies engaging muscle synergies improve motor control after spinal cord injury. *Nat. Med.* 22(2):138–45
79. Zhang Y, Zheng N, Cao Y, Wang F, Wang P, et al. 2019. Climbing-inspired twining electrodes using shape memory for peripheral nerve stimulation and recording. *Sci. Adv.* 5(4):eaaw1066
80. Cho KW, Lee WH, Kim B-S, Kim D-H. 2020. Sensors in heart-on-a-chip: a review on recent progress. *Talanta* 219:121269
81. Hong YJ, Jeong H, Cho KW, Lu N, Kim DH. 2019. Wearable and implantable devices for cardiovascular healthcare: from monitoring to therapy based on flexible and stretchable electronics. *Adv. Funct. Mater.* 29(19):1808247

82. Fang H, Yu KJ, Gloschat C, Yang Z, Song E, et al. 2017. Capacitively coupled arrays of multiplexed flexible silicon transistors for long-term cardiac electrophysiology. *Nat. Biomed. Eng.* 1(3):0038
83. Park J, Choi S, Janardhan AH, Lee S-YY, Raut S, et al. 2016. Electromechanical cardioplasty using a wrapped elasto-conductive epicardial mesh. *Sci. Transl. Med.* 8(344):344ra86
84. Choi S, Han SI, Jung D, Hwang HJ, Lim C, et al. 2018. Highly conductive, stretchable and biocompatible Ag-Au core-sheath nanowire composite for wearable and implantable bioelectronics. *Nat. Nanotechnol.* 13(11):1048–56
85. Sunwoo SH, Han SI, Kang H, Cho YS, Jung D, et al. 2020. Stretchable low-impedance nanocomposite comprised of Ag-Au core-shell nanowires and Pt black for epicardial recording and stimulation. *Adv. Mater. Technol.* 5(3):1900768
86. Gannarapu A, Gozen BA. 2016. Freeze-printing of liquid metal alloys for manufacturing of 3D, conductive, and flexible networks. *Adv. Mater. Technol.* 1(4):1600047
87. Guo R, Liu J. 2017. Implantable liquid metal-based flexible neural microelectrode array and its application in recovering animal locomotion functions. *J. Micromech. Microeng.* 27(10):104002
88. Wen X, Wang B, Huang S, Liu TL, Lee M-S, et al. 2019. Flexible, multifunctional neural probe with liquid metal enabled, ultra-large tunable stiffness for deep-brain chemical sensing and agent delivery. *Biosens. Bioelectron.* 131:37–45
89. Lee E, Kim HJ, Park Y, Lee S, Lee SY, et al. 2019. Direct patterning of a carbon nanotube thin layer on a stretchable substrate. *Micromachines* 10(8):530
90. Gilshteyn EP, Lin S, Kondrashov VA, Kopylova DS, Tsapenko AP, et al. 2018. A one-step method of hydrogel modification by single-walled carbon nanotubes for highly stretchable and transparent electronics. *ACS Appl. Mater. Interfaces* 10(33):28069–75
91. Song W-L, Gong C, Li H, Cheng X-D, Chen M, et al. 2017. Graphene-based sandwich structures for frequency selectable electromagnetic shielding. *ACS Appl. Mater. Interfaces* 9(41):36119–29
92. Zhao Z, Huang Q, Yan C, Liu Y, Zeng X, et al. 2020. Machine-washable and breathable pressure sensors based on triboelectric nanogenerators enabled by textile technologies. *Nano Energy* 70:104528

93. Ganji M, Elthakeb AT, Tanaka A, Gilja V, Halgren E, Dayeh SA. 2017. Scaling effects on the electrochemical performance of poly(3,4-ethylenedioxythiophene (PEDOT), Au, and Pt for electrocorticography recording. *Adv. Funct. Mater.* 27(42):1703018
94. Wang Y, Zhu C, Pfattner R, Yan H, Jin L, et al. 2017. A highly stretchable, transparent, and conductive polymer. *Sci. Adv.* 3(3):e1602076
95. Liu Y, Liu J, Chen S, Lei T, Kim Y, et al. 2019. Soft and elastic hydrogel-based microelectronics for localized low-voltage neuromodulation. *Nat. Biomed. Eng.* 3:58–68
96. Lu B, Yuk H, Lin S, Jian N, Qu K, et al. 2019. Pure PEDOT:PSS hydrogels. *Nat. Commun.* 10:1043
97. Wang H, Biswas SK, Zhu S, Lu Y, Yue Y, et al. 2020. Self-healable electro-conductive hydrogels based on core-shell structured nanocellulose/carbon nanotubes hybrids for use as flexible supercapacitors. *Nanomaterials* 10(1):112
98. Nam J, Lim HK, Kim NH, Park JK, Kang ES, et al. 2020. Supramolecular peptide hydrogel-based soft neural interface augments brain signals through a three-dimensional electrical network. *ACS Nano* 14(1):664–75
99. Lim C, Shin Y, Jung J, Kim JH, Lee S, Kim DH. 2019. Stretchable conductive nanocomposite based on alginate hydrogel and silver nanowires for wearable electronics. *APL Mater.* 7(3):031502
100. Du J, Wang L, Shi Y, Zhang F, Hu S, et al. 2020. Optimized CNT-PDMS flexible composite for attachable health-care device. *Sensors* 20(16):4523
101. Kim T, Park J, Sohn J, Cho D, Jeon S. 2016. Bioinspired, highly stretchable, and conductive dry adhesives based on 1D-2D hybrid carbon nanocomposites for all-in-one ECG electrodes. *ACS Nano* 10(4):4770–78
102. Matsuhisa N, Inoue D, Zalar P, Jin H, Matsuba Y, et al. 2017. Printable elastic conductors by *in situ* formation of silver nanoparticles from silver flakes. *Nat. Mater.* 16(8):834–40
103. Zhang Y, Xu S, Fu H, Lee J, Su J, et al. 2013. Buckling in serpentine microstructures and applications in elastomer-supported ultra-stretchable electronics with high areal coverage. *Soft Matter* 9(33):8062–70
104. Wang Y, Yin L, Bai Y, et al. 2020. Electrically compensated, tattoo-like electrodes for epidermal electrophysiology at scale. *Sci. Adv.* 6(43):eabd0996